Inorg. Chem. **2009**, *48*, 149−163

Stable and Highly Persistent Quinoxaline-Centered Metalloorganic Radical Anions: Preparation, Structural, Spectroscopic, and Computational Investigations

Sylvie Choua,* Jean-Pierre Djukic,* Jérôme Dalléry, André Bieber, Richard Welter,† Jean-Paul Gisselbrecht, Philippe Turek, and Louis Ricard†

Institut de Chimie de Strasbourg, CNRS, Université Louis Pasteur, 4 rue Blaise Pascal, 67000 Strasbourg, France, and Laboratoire Hétéro-Eléments et Coordination, CNRS, Ecole Polytechnique, route de Saclay, 91128 Palaiseau Cedex, France

Received July 30, 2008

Coordination of diazines such as quinoxaline to transition metals stabilizes radical anions generated by chemical or electrochemical cathodic reduction. However, even though various sorts of radical anionic diazines have been subjected to spectroscopic investigations in the recent past, reports combining structural, solid-state electron paramagnetic resonance (EPR) and computational investigations of kinetically stable species are still missing. In this study, four radical anions derived from tricarbonylmanganese- and tricarbonylrhenium-bound quinoxaline chelates, embedded within a triple-decker architecture, have been prepared from neutral substrates by chemical reduction over alkaline metals (K, Rb); the electronic structure of the latter metalloorganic paramagnetic salts was investigated by the means of structural X-ray diffraction analysis, electrochemistry, solution and crystal EPR spectroscopy, and density functional theory (DFT). Unprecedented structures of three manganese-bound and one rhenium-bound quinoxaline-derived paramagnetic salts were obtained from solutions of the corresponding radical anions crystallized in the presence of cryptand 222. It is inferred from a comparative study of the structures of anionic and neutral quinoxaline complexes that reduction does not have any significant impact over the coordination mode of the metal centers and over the overall geometry of the triple-decker architecture. The most notable changes in the radical-anionic metalloorganic species, as compared to the neutral parent molecules, comprise a slight hapticity shift of the metal-bound benzyl moiety and a weak intraannular distortion of the quinoxalyl core. Single-crystal EPR experiments carried out with the rhenium and manganese compounds produced the respective anisotropic **g** tensor, which was found in each case to be essentially located at the quinoxalyl fragment. Computations, carried out using DFT methods (B3LYP−LANL2DZ and Becke−Perdew−TZP), corroborated the features suggested by structural analysis. Single-point calculation using the B3LYP functional and various basis sets [LANL2DZ, 6-31G(d), 6-311+G(d), and 6-311+G(2d,p)] provided us with values of anisotropic **g** tensors and hyperfine coupling constants consistent with those determined experimentally. It is inferred from this study that the two metal centers bound to the nitrogen atoms of the quinoxalyl core contribute in the lowering of the HOMO−LUMO gap in the neutral species. The triple-decker arrangement, which combines chelation of the metal, steric protection, and encapsulation of the central quinoxalyl core, is a stabilizing factor that provides a long-lived character to the radical-anionic species.

Introduction

Recently, there has been a particular upsurge of interest for applications of so-called diazines in the field of organic electronics. The rising number of patents dealing with applications of diazines in the latter domain reflects the growing demand for robust molecules capable of undergoing repeated uptake and release of electrons. Owing to their marked electron affinity,[1,2] diazines have proven to be effective for electron transport[3,4] and storage[5] in either

* To whom correspondence should be addressed. E-mail choua@chimie.u-strasbg.fr (S.C.), djukic@chimie.u-strasbg.fr (J.-P.D.). Phone: +33(0)390241623(S.C.), +33(0)390241523(J.-P.D.).

† For requests pertaining to the crystallographic structural determination of [K(222)][**3a**]·THF, [Rb(222)][**3a**]·THF, [Rb(222)][**3a**], and [K(222)][**3c**] should be addressed, contact the following: e-mail, louis.ricard@polytechnique.edu; phone, +33(0)169334413. For other structures, refer to the following: e-mail, welter@chimie.u-strasbg.fr; phone, +33(0)390241593.

(1) Lottermoser, U.; Rademacher, P.; Mazik, M.; Kowski, K. *Eur. J. Org. Chem.* **2005**, 522–531.

(2) Casu, M. B.; Imperia, P.; Schrader, S.; Falk, B.; Jandke, M.; Strohriegl, P. *Synth. Met.* **2001**, *124*, 79–81.

10.1021/ic801434h CCC: $40.75
Published on Web 12/03/2008

oligomeric or polymeric[6−11] forms. Diazines can indeed be reduced by successive one-electron processes to produce radical anions and dianions, whose reactivity and structural stability is subject to structural alterations.[12] Even though the spectroscopic properties of salts of organic radical anions have received a great deal of attention,[13] only a few examples of structures of paramagnetic radical-anionic diazines obtained from single-crystal X-ray diffraction analysis have been reported to date.[14] As a matter of fact, investigation of the physical properties has been hampered by the strong cathodic electrochemical potentials required to initiate electron uptake and to generate adequately spin density at the heterocycle. As a consequence, organic radical anions of diazines are generally short-lived because of kinetic instability.[15] A strategy consisting of raising the reduction potential to "accessible" cathodic potentials by tuning the level of the lowest unoccupied molecular orbital (LUMO) by coordination of the donor nitrogen atoms of a diazine ligand to transition-metal centers has been granted quite a large interest,[16−18] and the consequences of delocalization of the spin density all over the ligand and metal have been broadly investigated,[19−22] having in view application to the catalysis of carbon dioxide reduction for instance.[23] Such radical-anionic coordination complexes belong to Olbrich-Deussner and Kaim's[24] class of so-called "18 + δ" complexes,[25,26] in which the spin density resides "mostly" at the aromatic ligand. It has been proposed that a highest occupied molecular orbital (HOMO)−LUMO gap lower than 1 eV and a cathodic reduction potential higher than −1 V/saturated calomel electrode (SCE) have proven necessary to ensure sufficient persistence of "18 + δ" radical anions.[27] The lability of the metal−nitrogen bond in radical-anionic diazine coordination complexes[28] is an issue that may confine characterization of the paramagnetic species to solution analyses. It has been recently shown that chelation of the metal center increases the overall persistence of a radical anion generated by reduction of a quinoxaline coordination complex of rhenium(I), which proved to be electron paramagnetic resonance (EPR)-detectable and, moreover, persistent in solution.[29] Helical $\eta^2-\eta^1$-benzylorganomanganese[30] triple-decker systems synthesized by the stereospecific coupling of biscyclometalated heterocyclic compounds such as **2a**[31] (Scheme 1) with aryldiazomethanes were also found to produce persistent radical anions upon chemical reduction in solution.[32] This peculiar class of organometallic complexes, among which **3a** is the first prototype (Scheme 1), has opened the way to further investigations of the physical and structural properties of the corresponding radical-anionic diazines.[33,34]

Scheme 1

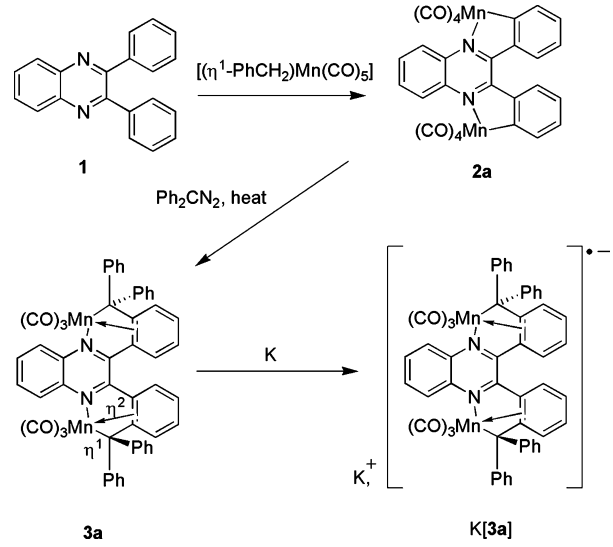

EPR spectroscopy has proven its efficiency in the study of the electronic structure of a series of reduced α-diimine $Re(CO)_3$ halide derivatives.[16,35,36] Density functional theory

(3) Casu, M. B.; Imperia, P.; Schrader, S.; Schulz, B.; Jandke, M.; Strohriegl, P. *Synth. Met.* **2001**, *121*, 1397–1398.
(4) Imperia, P.; Casu, M. B.; Schrader, S.; Falk, B.; Jandke, M.; Strohriegl, P. *Synth. Met.* **2001**, *121*, 1673–1674.
(5) Nakagawa, Y.; Nishiyama, T.; Kamisuki, H.; Harada, G.; Kaneko, S.; Kurosaki, M.; Nobuta, T.; Mitani, M. (NEC Tokin Corp.). U.S. Patent 6,678,150 B2, 2004.
(6) Saito, N.; Yamamoto, T. *Synth. Met.* **1995**, *69*, 539–540.
(7) Kanbara, T.; Inoue, T.; Sugiyama, K.; Yamamoto, T. *Synth. Met.* **1995**, *71*, 2207–2208.
(8) Thelakkat, M.; Schmidt, H. W. *Polym. Adv. Technol.* **1998**, *9*, 429–442.
(9) Petit, M. A.; Clarisse, C.; Templier, F. *J. Electrochem. Soc.* **1993**, *140*, 2498–2500.
(10) Giebeler, C.; Marks, R. N.; Bleyer, A.; Bradley, D. D. C.; Schrader, S. *Opt. Mater.* **1998**, *9*, 99–103.
(11) Yamamoto, T.; Hayashida, N. *React. Funct. Polym.* **1998**, *37*, 1–17.
(12) Cohen, Y.; Meyer, A. Y.; Rabinovitz, M. *J. Am. Chem. Soc.* **1986**, *108*, 7039–7044.
(13) Gerson, F.; Huber, W. *Electron Spin Resonance Spectroscopy of Organic Radicals*; Wiley-VCH: Weinheim, Germany, 2003.
(14) Bock, H.; John, A.; Naether, C.; Ruppert, K. *Helv. Chim. Acta* **1994**, *77*, 1505–1519.
(15) O'Reilly, J. E.; Elving, P. J. *J. Am. Chem. Soc.* **1972**, *94*, 7941–7949.
(16) Kaim, W. *Coord. Chem. Rev.* **2002**, *230*, 127–139.
(17) Ward, M. D. *Chem. Soc. Rev.* **1995**, 121–134.
(18) Kaim, W. *Coord. Chem. Rev.* **1987**, *76*, 187–235.
(19) Kaim, W. *Inorg. Chem.* **1984**, *23*, 3365–3368.
(20) Kaim, W.; Kohlmann, S. *Inorg. Chem.* **1986**, *25*, 3442–3448.
(21) Klein, A.; E. J. L., M.; Scheiring, T.; Zalis, S. *J. Chem. Soc., Faraday Trans.* **1998**, *94*, 2979–2984.
(22) Kaim, W.; Klein, A.; Glöckle, M. *Acc. Chem. Res.* **2000**, *33*, 755–763.
(23) Rasmussen, S. C.; Richter, M. M.; Yi, E.; Place, H.; Brewer, K. J. *Inorg. Chem.* **1990**, *29*, 3926–3932.
(24) Olbrich-Deussner, B.; Kaim, W. *J. Organomet. Chem.* **1988**, *340*, 71–91.
(25) Klein, A.; Vogler, C.; Kaim, W. *Organometallics* **1996**, *15*, 236–244.
(26) Tyler, D. R. *Acc. Chem. Res.* **1991**, *24*, 325–331.
(27) Meyer, R.; Schut, D. M.; Keana, K. J.; Tyler, D. R. *Inorg. Chim. Acta* **1995**, *240*, 405–412.
(28) Gross, R.; Kaim, W. *Inorg. Chem.* **1986**, *25*, 498–506.
(29) Das, A. K.; Bulak, E.; Sarkar, B.; Lissner, F.; Schleid, T.; Niemeyer, M.; Fiedler, J.; Kaim, W. *Organometallics* **2008**, *27*, 218–223.
(30) Djukic, J. P.; Dötz, K. H.; Pfeffer, M.; De Cian, A.; Fischer, J. *Organometallics* **1997**, *16*, 5171–5182.
(31) de Cian, A.; Djukic, J. P.; Fischer, J.; Pfeffer, M.; Dötz, K. H. *Chem. Commun.* **2002**, 638–639.
(32) Djukic, J. P.; Michon, C.; Maisse-François, A.; Allagapen, R.; Pfeffer, M.; Dötz, K. H.; De Cian, A.; Fischer, J. *Chem.—Eur. J.* **2000**, *6*, 1064–1077.
(33) Michon, C.; Djukic, J.-P.; Ratkovic, Z.; Collin, J.-P.; Pfeffer, M.; de Cian, A.; Fischer, J.; Heiser, D.; Doetz, K. H.; Nieger, M. *Organometallics* **2002**, *21*, 3519–3535.
(34) Djukic, J.-P.; Michon, C.; Ratkovic, Z.; Kyritsakas-Gruber, N.; De Cian, A.; Pfeffer, M. *Dalton Trans.* **2006**, 1564–1573.
(35) Andrea, R. R.; De Lange, W. G. J.; Van der Graaf, T.; Rijkhoff, M.; Stufkens, D. J.; Oskam, A. *Organometallics* **1988**, *7*, 1100–1106.
(36) Frantz, S.; Fiedler, J.; Hartenbach, I.; Schleid, T.; Kaim, W. *J. Organomet. Chem.* **2004**, *689*, 3031–3039.

Scheme 2

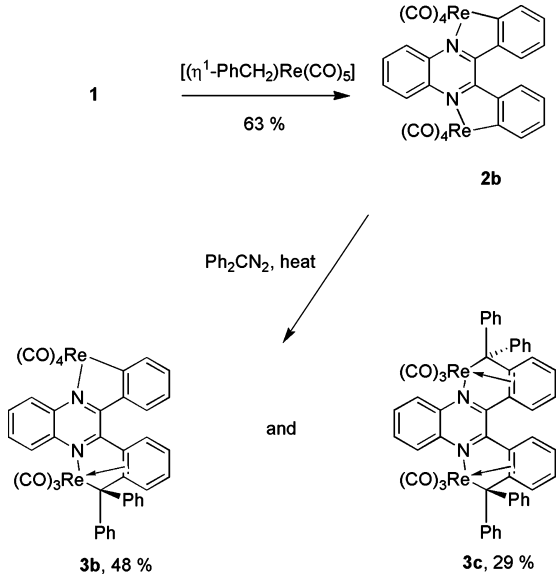

(DFT) calculations combined with high-field EPR analyses provide sound ground for discussions.[37,38] The relevant parameters with respect to EPR are the **g** tensor and the hyperfine coupling constants (hfcc's), with the latter being on hand through DFT calculations. Not always available is structural information on reduced complexes, which are essential to verify the pertinence of computations. In this Article, we report on the complete structural and spectroscopic characterization of stable quinoxaline-based radical-anionic triple-decker helical complexes containing manganese(I) tricarbonyl and rhenium(I) tricarbonyl scaffolds. We also provide details of the investigation of their electronic structure by the methods of DFT and elaborate on the effect of the metal centers over spin delocalization.

Results and Discussion

Synthesis of 3c. The synthesis of the rhenium analogue of **3a**, i.e., **3c**, was carried out using the same strategy as that for **3a**, with the first step being the cyclorhenation of 1,2-diphenylquinoxaline **1**, followed by the condensation of 1,1-diphenyldiazomethane with the biscyclorhenated compound **2b** synthesized in the first instance. Cyclorhenation reactions using (η^1-$PhCH_2$)$Re(CO)_5$ expectedly required long reaction times, i.e., around 10 h, to complete. Careful monitoring of the reaction mixture by IR spectroscopy was necessary to ensure that full metalation of the ligand occurred. The reaction between 2,3-diphenylquinoxaline **1** and a large excess of (η^1-$PhCH_2$)$Re(CO)_5$ in refluxing toluene yielded the biscyclorhenated product **2b** (Scheme 2) as the major product. The molecular structure of compound **2b** was satisfactorily established by X-ray diffraction analysis (cf. the Supporting Information). Complex **2b** consists of two symmetry-related enantiomeric helical *M* and *P* forms in the crystal lattice. The helicity of these enantiomers stems from the steric hindrance mutually exerted by vicinal phenylene moieties and can be quantified by an interplanar phenylene−phenylene angle of 58.3°. This angle is weaker than that in the parent compound resulting from the biscyclomanganation of 2,3-diphenylbenzo[*g*]quinoxaline (63.7°).[39] In the crystal lattice, molecules of **2b** are π-stacked almost in a parallel head-to-tail manner with alternation of *M* and *P* isomers. The mean intermolecular quinoxalyl-to-quinoxalyl fragment distance amounts to 3.8 Å. It was found, in agreement with previous findings, that to achieve the double condensation of 1,1-diphenyldiazomethane with **2b**, the use of a very large excess of diazoalkane was necessary. The reason for this lies in the pace of the condensation reaction, which depends on how effective the formation of the rhenium−carbene intermediate is and on its evolution by insertion into the C−Re bond of the chelate. If these steps are slow, given the high temperature at which the process is promoted, the classical decomposition of Ph_2CN_2 into tetraphenylethene and diazines becomes a competitive process. Under the experimental conditions used in this study, the reaction of dinuclear complex **2b** with 20 equiv of Ph_2CN_2 in boiling toluene (Scheme 2) still afforded a mixture of two complexes, i.e., **3b** and **3c**, which were separated by chromatography on SiO_2 at low temperature. To avoid the burden of a tedious separation of organic decomposition products, we restrained the amount of diazoalkane to 20 equiv. Compounds **3b** and **3c** (vide infra) were isolated respectively as air-stable brown and dark-brown powders, which were fully characterized analytically and structurally analyzed by X-ray diffraction. Spectroscopic and analytical data, complemented with structural X-ray diffraction analysis (cf. the Supporting Information), ascertained that **3b** originates from the decarbonylative single condensation of a diphenylmethylidene moiety with **2b**.

Structural X-ray Diffraction Analysis of Neutral 3c. Figure 1 displays the molecular structure of **3c**. The most notable geometric differences between **3a**[33] and **3c** are essentially the metal-to-carbon and metal-to-nitrogen distances, which are longer in **3c** by ca. 0.13 Å as compared to distances Mn−C and Mn−N in **3a** (vide infra Table 6). Similarly to **3a**, the racemic nature of **3c** can be verified by the alternation of homochiral layers of (*M*,*M*)-**3c** and (*P*,*P*)-**3c** (Figures 1 and 2).

Electrochemical and Spectroelectrochemical Behavior of 3c. The electrochemical investigation of **3c** was carried out in dichloromethane and in acetonitrile. Species **3c** undergoes two reversible one-electron-reduction steps. This behavior is similar to that previously reported for **3a**[33] for which the reduction was one-electron-wise and reversible, leading to fully reversible **3a**/**3a**$^-$ and **3a**$^-$/**3a**$^{2-}$ redox couples. The electrochemical data of **3c** as well as those of species **1** and **3a** are provided in Table 2 for comparison. A large potential shift to less negative values as compared to

(37) Frantz, S.; Hartmann, H.; Doslik, N.; Wanner, M.; Kaim, W.; Kuemmerer, H.-J.; Denninger, G.; Barra, A.-L.; Duboc-Toia, C.; Fiedler, J.; Ciofini, I.; Urban, C.; Kaupp, M. *J. Am. Chem. Soc.* **2002**, *124*, 10563–10571.

(38) Sarkar, B.; Frantz, S.; Kaim, W.; Duboc, C. *Dalton Trans.* **2004**, 3727–3731.

(39) Djukic, J. P.; De Cian, A.; Kyritsakas-Gruber, N. *J. Organomet. Chem.* **2005**, *690*, 4822–4827.

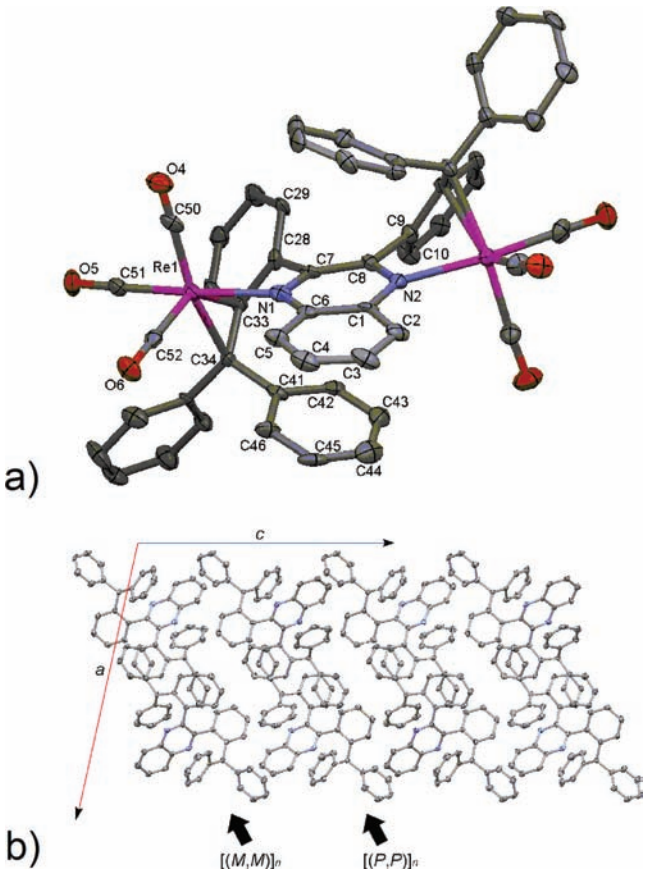

Figure 1. (a) CCDC Mercury "ellipsoid" view of compound **3c** drawn at 40% probability with a partial atom numbering scheme. Hydrogen atoms and solvent have been omitted for clarity. Selected interatomic distances (Å): Re1−N1 2.181(6), Re1−C34 2.260(7), Re1−C33 2.360(6), Re1−C28 2.553(7). Selected angle (deg): C34−Re1−C51 95.8(3). Torsion angles (deg): C29−C28−C7−C8 51.21, C7−C8−C9−C10 46.64. Angle between mean planes P_1 (N1−C7−C8−N2−C1−C2−C3−C4−C5−C6) and P_2 (C41−C42−C43−C44−C45−C46) (deg): 18.33. (b) Projection along crystallographic axis *b* of the packing scheme in the crystal lattice.

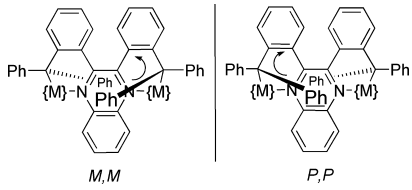

Figure 2. Compounds **3a** and **3c** are racemic mixtures of *M*,*M* and *P*,*P* enantiomers. The *M* and *P* descriptors of chirality refer to the helicity of the two helical organometallic fragments that encapsulate the quinoxalinyl core.

the bare ligand **1** was noted. The first reduction potentials of **3a** and **3c** in dichloromethane were found at potentials of 640 and 890 mV higher than the corresponding one-electron-reduction potential of ligand **1**. Such large potential shifts were also observed for rhenium tetrazine complexes.[40] Quite unexpected was the marked difference of 250 mV existing between the potentials of couples **3a** /**3a**$^-$ and **3c** /**3c**$^-$, which somewhat suggests that the electronegativity of the metal is relevant as to the overall stabilization of the radical-anionic species.

(40) Frantz, S.; Kaim, W.; Fiedler, J.; Duboc, C. *Inorg. Chim. Acta* **2004**, *357*, 3657–3665.

Proof of the electrochemical reversibility of the reduction of **3c** was provided by subsequent spectroelectrochemical studies in a homemade optically transparent thin-layer electrode (OTTLE) cell. A time-resolved UV−visible spectrum of **3c** was recorded in dichloromethane by sweeping forward and backward the potential of the working electrode (Figure 3) stepwise from 0 to −1.3 V vs Fc^+/Fc. A similar experiment carried out with **3a** confirmed earlier results (see the Supporting Information). The main UV−visible maxima and isosbestic points are summarized in Table 3. In all cases, the initial spectrum was recovered flawlessly and quantitatively upon reoxidation of the electrogenerated species. These neutral and monoreduced species display transitions with different extinction coefficients, which are putatively assigned to metal-to-ligand charge-transfer (MLCT) transitions around 500 nm (Table 3). Two additional electronic transitions in the near-IR region (854 and 970 nm) were observed only in the absorption spectrum of **3c**$^-$ (Table 3). To complete the picture, it must be noted that the chemical reduction with potassium in tetrahydrofuran (THF) of either **3a** or **3c** into **3a**$^-$ or **3c**$^-$ led to only minor changes for the C−O bond elongation-related bands, with the A_1 and E bands being shifted by less than 10 cm^{-1} toward lower frequencies.

Preparation of [(222)K][3a] and [(222)K][3c] and the Structural Characterization of [(222)K]3a·THF and [(222)K]3c. In a glovebox, THF solutions containing an equimolar mixture of either **3a** or **3c** and cryptand 222 were reduced over a clean potassium mirror deposited in a sample glass tube (eq 1). The resulting solutions were then transferred to clean glass tubes, and a layer of dry *n*-pentane was subsequently added. The tubes were stopped, and the layers were left to diffuse at room temperature.

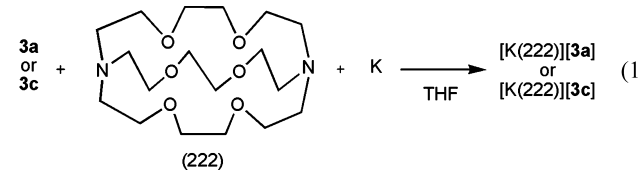

(1)

Both potassium salts crystallized in the triclinic system, with their crystal lattice fitting the $P\bar{1}$ space group (Table 1). Figures 4 and 5 display CSD Mercury diagrams of the asymmetric unit in each unit cell and views of the molecular packing in the crystal lattice. At the molecular level, the main difference between the structures of these two salts resides in the peculiar interaction established between the chelated potassium center and one rhenium-bound carbonyl ligand, which is not observed with the manganese analogue [K(222)][**3a**]·THF. This interaction is characterized by an interatomic distance between the terminal oxygen atom O1 and the potassium cation K1 of 2.900(5) Å. The molecular packing in [K(222)][**3a**]·THF and [K(222)][**3c**] differs in the way that *M*,*M* and *P*,*P* enantiomers are arranged. With the organomanganese salt, there is an alternation of homochiral layers parallel to the crystallographic *b* axis. Within each individual homochiral layer, molecular units are stacked in a columnar manner. Within a single homochiral column aligned along the *b* axis, the shortest distance between two

Table 1. Acquisition Parameters and Refinement Data for the Resolution of the Structures of **2b**, **3b**, **3c**, [K(222)][**3a**]·THF, [Rb(222)][**3a**]·THF, [Rb(222)][**3a**], and [K(222)][**3c**]

	2b	**3b**	**3c**	[K(222)][**3a**]·THF [a]	[Rb(222)][**3a**]·THF [a]	[Rb(222)][**3a**]	[K(222)][**3c**]
formula	$C_{28}H_{12}N_2O_8Re_2$	$C_{41}H_{24}Cl_2N_2O_7Re_2$	$C_{56}H_{42}N_2O_8Re_2$	$C_{52}H_{32}Mn_2N_2O_6$,$C_{18}H_{36}N_2O_6K$, C_4H_8O	$C_{52}H_{32}Mn_2N_2O_6$, $C_{18}H_{36}N_2O_6Rb$, C_4H_8O	$C_{70}H_{68}Mn_2N_4O_{12}Rb$	$C_{70}H_{68}KN_4O_{12}Re_2$
fw	876.80	1099.92	1243.32	1378.37	1424.74	1352.63	1568.78
cryst dimen	0.20 × 0.10 × 0.10	0.09 × 0.08 × 0.07	0.10 × 0.10 × 0.08	0.22 × 0.22 × 0.16	0.20 × 0.18 × 0.16	0.20 × 0.20 × 0.05	0.22 × 0.19 × 0.05
cryst syst	monoclinic	triclinic	monoclinic	triclinic	triclinic	triclinic	triclinic
space group	$P2_1/c$	$P\bar{1}$	$P2_1/c^-$	$P1$	$P\bar{1}$	$P\bar{1}$	$P\bar{1}$
a (Å)	14.6930(3)	12.016(2)	20.8750(11)	13.659(1)	13.659(1)	9.940(1)	9.975(1)
b (Å)	13.0870(3)	12.949(2)	12.0170(9)	15.838(1)	15.847(1)	17.573(1)	17.635(1)
c (Å)	13.3260(4)	13.764(3)	19.0610(12)	17.601(1)	17.651(1	20.179(1)	20.347(1)
α (deg)	90.00	101.64(5)	90.00	65.824(1)	65.858(1)	66.025(1)	65.784(1)
β (deg)	90.930(1)	102.18(5)	102.435(5)	84.832(1)	84.602(1)	79.711(1)	80.100(1)
γ (deg)	90.00	112.15(5)	90.00	75.635(1)	75.724(1)	89.103(1)	89.374(1)
V (Å^3)	2562.1(1)	1842.9(13)	4669.4(5)	3364.8(4)	3378.7(4)	3162.5(4)	3208.6(4)
Z	4	2	4	2	2	2	2
D_{calcd} (g·cm^{-3})	2.273	1.982	1.769	1.289	1.400	1.420	1.624
μ(Mo Kα) (mm^{-1})	9.497	6.762	5.240	5.000	1.157	1.230	3.900
T (K)	173(2)	173(2)	173(2)	150.0(1)	150.0(1)	150.0(1)	150.0(1)
θ_{max}	30.02	30.03	27.86	30.06	30.00	27.50	27.48
unique data, R(int)	5743, 0.0644	8148, 0.0325	6628, 0.0654	19599, 0.0198	19653, 0.0233	14463, 0.0307	14052, 0.0424
obsd data	2σ(I)	2σ(I)	2σ(I)	2σ(I)	2σ(I)	2σ(I)	2σ(I)
N_{refins}, N_{params}	7480, 361	10 633, 487	11 118, 613	14 843, 803	14 356, 802	10 606, 802	10 464, 803
R1	0.0390	0.0425	0.0579	0.0421	0.0380	0.0368	0.0431
wR2	0.1022	0.1050	0.0979	0.1337	0.1119	0.0882	0.1193
GOF	1.171	1.049	0.983	1.087	1.018	1.004	1.043

[a] A highly disordered THF molecule that could not be properly resolved was accounted for using the Platon SQUEEZE function.

neighboring quinoxalyl cores amounts to ca. 13 Å. The shortest intermolecular distance between two organometallic moieties of ca. 3.5 Å corresponds to C−H···π contacts between two perpendicular *exo*-phenyl fragments. The shortest distances between two quinoxalyl cores that belong to different columns of the same homochiral layer amount to ca. 11 Å. In this case, two homochiral organometallic columns are separated by a column of K(222) units. With the rhenium salt, layers of homochiral salts are parallel to the crystallographic *a* axis and are periodically interleaved with a layer of salts possessing the opposite stereochemistry. Within a single layer, organometallic anions are stacked in a perfect columnar manner along the *a* axis. In this case, the shortest intermolecular distances of 3.8−3.9 Å correspond to short parallel interactions between a quinoxalyl core with the *endo*-phenyl group of a neighboring molecule. In other terms, each homochiral layer contains parallel arrays of columns of [K(222)][**3c**].

Reduction of 3a with Rubidium in the Presence of Cryptand 222, the "Solvatomorphism" of [Rb(222)][3a] in the Solid State. Metallic rubidium was also used as a reducing agent with compound **3a** in order to assess the effect of the nature of the countercation on crystal packing and nucleation (Scheme 3). The reduction of **3a** was carried out in conditions similar to those described with the potassium metal and cryptand 222. Crystallizations by the slow diffusion of a THF solution of [Rb(222)][**3a**] in *n*-pentane produced two types of crystals, both crystallizing in the triclinic system and $P\bar{1}$ space group according to X-ray diffraction analysis. A first crystal was found to be nearly isostructural with [K(222)][**3a**]·THF and was formulated as [Rb(222)][**3a**]·THF (Figure 6a). A second crystal was found to be nearly isostructural with [K(222)][**3c**] and was formulated as [Rb(222)][**3a**] (Figure 6b).

This observed isostructurality is supported by nearly equal unit cell parameters and by similar if not identical geometries and distortions of the molecular components within the respective unit cells (Table 1). These observations suggest inter alia that the coordination of the potassium cation to the terminal oxygen of a carbonyl ligand in [K(222)][**3c**] is not specific to this rhenium compound. It seemingly relates to the mechanism of nucleation in the chosen system of solvents.

Single-Crystal EPR. The principal values of the **g** tensor of compounds [K(222)][**3a**] and [K(222][**3c**] were determined upon rotation of the single crystals of [K(222)][**3a**]·THF and [K(222][**3c**] previously analyzed by structural X-ray diffraction, within three mutually orthogonal planes (Figure 7 and the Supporting Information).[41] The connection between laboratory and crystallographic axes could not be assessed with the EPR experimental setup, allowing only a rough manual manipulation of the crystals. Moreover, the crystals were tiny and embedded in protective oil, difficulties to be added to their low triclinic symmetry. Therefore, the relationships between the crystal axes and the **g**-tensor principal axes could not be determined. The

(41) Wertz, J. E.; Bolton, J. R. In *Electron Spin resonance—Elementary Theory and Practical Applications*; Chapman and Hall Ltd.: London, 1986; p 131.

Table 2. Reduction Potentials Measured at Room Temperature with 10^{-4} or 10^{-3} M Solutions in the Presence of Ferrocene[a]

	1	**3a**		**3c**	
solvent	CH_2Cl_2 [b]	CH_3CN	CH_2Cl_2	CH_3CN	CH_2Cl_2
scan rate [c]	100	100	100	100	100
E'° [d] (ΔE_p) [e]	−2.09 (75)	−1.30 (60), −2.02 (65), −2.34 (130)	−1.45 (70), −2.20 (70)	−1.08 (60), −2.02 (60)	−1.20 (60), −2.19 (70)

[a] All potentials are given versus Fc^+/Fc used as an internal standard. [b] From ref 56. [c] In $mV \cdot s^{-1}$. [d] In V. [e] $|E_{pc} - E_{pa}|$ in mV.

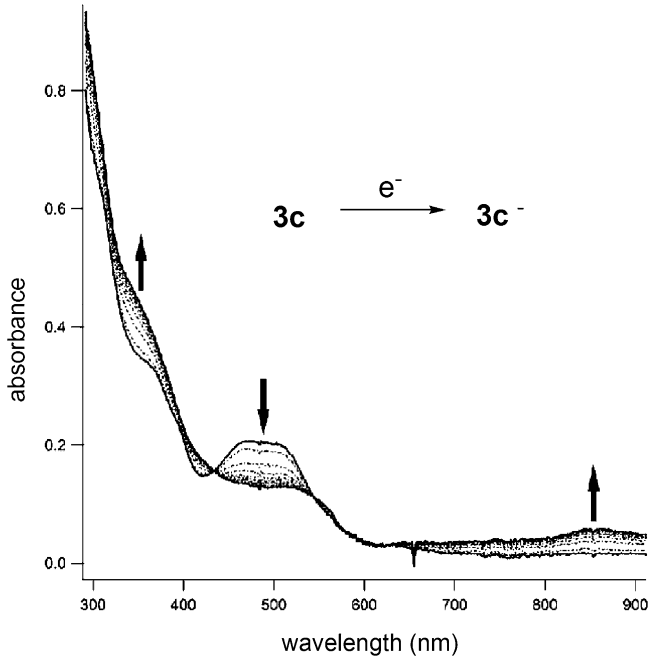

Figure 3. Time-resolved UV−visible spectroelectrochemical experiments in CH_2Cl_2: arrows indicate the evolution of the absorption bands upon reduction of **3c** into **3c**$^-$.

Table 3. UV−Visible Absorption Data from the Spectroelectrochemical Studies of **3a** and **3c** in CH_2Cl_2

compound	λ_{max} (nm)	isosbestic points (nm)
3a	347, 437 (sh), 572	
		376, 536, 695
3a$^-$	340, 448 (sh), 544 (sh)	
3c	360 (sh), 472, 506	
		435, 545, 570
3c$^-$	351 (sh), 512, 854, 970	

temperature dependence of the EPR properties was studied within the 4−100 K range along an orientation corresponding to a minimum line width so as to enhance the signal-to-noise ratio (Figure 8 and the Supporting Information). All spectra are symmetrical single lines. The position of the extrema of the $g(\theta)$ curves was observed to be unchanged upon checking of the angular dependence of single crystals at 4 K. Therefore, phase transition seems unlikely.

While both compounds exhibited the Curie behavior of isolated spin species (cf. the Supporting Information), they were quite different with respect to their local magnetic properties as probed through EPR (cf. the Supporting Information). The average value of the g factor of [K(222)][**3a**] was close to the free electron value (g_{av} = 2.0064); the EPR line width was quite narrow, and it was almost temperature independent between room temperature and 4 K. This behavior has to be related to that of a free organic radical. The average value of the g factor of [K(222)][**3c**] was shifted from the free electron value (g_{av} = 2.0144); the EPR line width was much larger, ca. 8 times larger, than that for [K(222][**3a**], and it broadened as the temperature was decreased.

Solution EPR. Solution EPR experiments were carried out with **3a** and **3c**, from which radical anions were generated chemically and electrochemically in a few cases. To assess the role of the metal within these complexes with and without cryptand 222 and to parallel the DFT calculations, we also generated radical anion **1**$^-$ from 2,3-diphenylquinoxaline **1** by reduction over a droplet of rubidium at room temperature in the presence of cryptand 222 (eq 2).

$$\mathbf{1} + Rb \xrightarrow[THF]{(222)} [Rb(222)][\mathbf{1}] \qquad (2)$$

The EPR and ENDOR study of **1**$^-$ was previously reported by Bock et al.[14] In the present study, a better resolved EPR spectrum was measured for [Rb(222)][**1**] as compared to that previously reported for K[**1**] by the latter authors. All hyperfine coupling constants were resolved without the assistance of ENDOR spectroscopy. The simulation of the EPR spectrum of [Rb(222)][**1**] in a frozen solution assumed two equivalent ^{14}N nuclei with an almost axial anisotropic tensor (Table 5).

As previously reported,[33] the reaction of **3a** with a potassium mirror in THF yielded a well-resolved EPR spectrum exhibiting the hyperfine pattern corresponding to two ^{55}Mn nuclei ($I = {}^5/_2$), two ^{14}N nuclei ($I = 1$), and two pairs of α and β protons in the 5,8 and 6,7 positions on the quinoxaline moiety (Table 4). The same spectrum was observed upon electrochemical generation of the radical anion **3a**$^-$ when an electrolysis was carried out around the first potential of the **3a**/**3a**$^-$ couple. When the temperature was decreased to 120 K, a single broad envelope was observed (line width ∼ 30 G) and simulated with the principal values of the **g** tensor determined from single-crystal experiments. The addition of cryptand 222 led to the same spectrum in fluid and frozen solutions. Further electrolysis at a potential corresponding to that of the **3a**$^-$/**3a**$^{2-}$ couple, i.e., at a potential about 760 mV more cathodic than that for the **3a**/**3a**$^-$ couple, did not reveal any signal typical of a biradical but rather a residual signal of **3a**$^-$.

The radical anion of **3c**$^-$ was generated with a potassium mirror in the presence and in the absence of cryptand 222. The effect of the latter on the EPR spectrum was similar to that described for **1**$^-$, i.e., a narrowing line enhancing the spectrum resolution (Figure 9). In both cases, the EPR spectrum in fluid solution exhibited three isotropic coupling constants of the pairs of α and β protons and two ^{14}N nuclei (Figure 9 and Table 4). Apart from minor variations of the isotropic coupling constants, this is very similar to the spectrum of radical anion K[**1**] that was obtained by reduction over a potassium mirror. In contrast to the manganese-containing radical anion **3a**$^-$, no additional hyperfine splitting could be ascribed to the metal center, i.e., to the $^{185,187}Re$ isotopes.

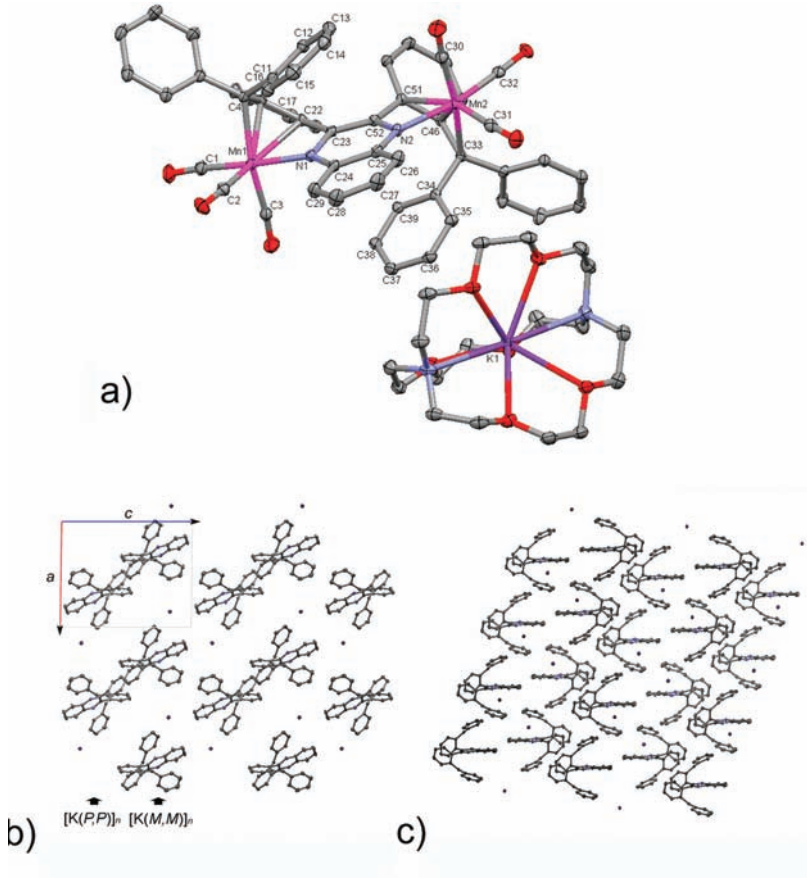

Figure 4. (a) CSD Mercury diagram of the structure of [K(222)]**3a**·THF drawn at the 30% probability level: atoms of hydrogen and molecules of THF have been omitted for clarity. (b) Crystal lattice projection along the crystallographic *b* axis showing the alternation of enantiomorphic sheets of (*P*,*P*)-[K(222)]**3a** and (*M*,*M*)-[K(222)]**3a**: atoms of hydrogen, *exo*-phenyl groups, $Mn(CO)_3$ moieties, and cryptand 222 have been omitted for clarity. (c) View of the crystal lattice showing the parallel and oblique-columnar arrangement of quinoxalyl cores interleaved with potassium centers: atoms of hydrogen, *exo*-phenyl groups, $Mn(CO)_3$ moieties, and cryptand 222 have been omitted for clarity.

Decreasing the temperature resulted in a broadening of the lines, and the frozen solution spectra were found to be similar in the presence or absence of cryptand 222. Only an unresolved signal was observed for **3c**$^-$. Attempts to simulate this spectrum using the **g** tensor deduced from the single-crystal study were not successful.

According to the differences in the observed EPR spectra in the presence of cryptand, the latter has an effect on (i) the line width in solution for **1**$^-$ and **3c**$^-$, resulting in a narrowing, and hence a better, resolution of the EPR spectra, and (ii) the **g** tensor and the line width of [K(222)][**3c**] in the solid state, resulting in a shift of the **g** tensor and a broadening line, as compared to [K(222)][**3a**]. In fluid solution, some spin density on Mn nuclei is required to interpret the EPR spectrum of [K(222)][**3a**], while Re nuclei's contribution is not necessary to simulate the EPR spectrum of [K(222)][**3c**]. This is contradictory with the properties in the solid state, where Mn is apparently silent in [K(222)][**3a**], leaving an almost free ligand-centered radical being, as opposed to [K(222)][**3c**], with a quite anisotropic **g** tensor as inferred from single-crystal studies. The EPR spectra in fluid solution point to an almost free organic radical for all compounds, whether incorporating cryptand 222 or not, as ascertained by the DFT computations (vide infra), which do not include the solvent, the cation, or the cryptand. This situation remains unchanged for [K(222)][**3a**] in the crystalline state. As a matter of fact, the molecular geometry of [K(222)][**3a**] in the crystal is close to the one optimized in DFT calculations in the absence of cryptand. This is not true for the crystal of [K(222)][**3c**] as compared to the "in vacuo"-computed molecular geometry: X-ray diffraction analysis indicates a specific interaction of the caged-potassium cation with one rebound CO ligand that induces a significant distortion of the organic backbone in the vicinity of the rhenium center that lifts the pseudo-C_2 symmetry of the organometallic radical anion. Without other supporting elements for the discussion of this effect, it is inferred that this peculiar interaction is promoting the role of rhenium in the **g** tensor and in the line width (through relaxation time), hence being an exception within the overall context.

DFT Computations of Triple-Decker Compounds 3a−c and 3a−c$^-$ in the Gas Phase. Geometry Optimization and Electronic Structure. Full geometry optimizations were performed without any symmetry restriction in order to provide the best model for the description of the ground-state electronic structure and bonding properties, while preserving the helical architecture of the complexes. For the sake of clarity, computed structures are named with roman numerals, i.e., **1** as **I**, **3a** as **IIIa**, and **3c** as **IIIc**. Computations were carried out using *Gaussian 03* (abbreviated G03)[42] and Amsterdam Density Functional 2003.01[43] (abbreviated ADF) packages.

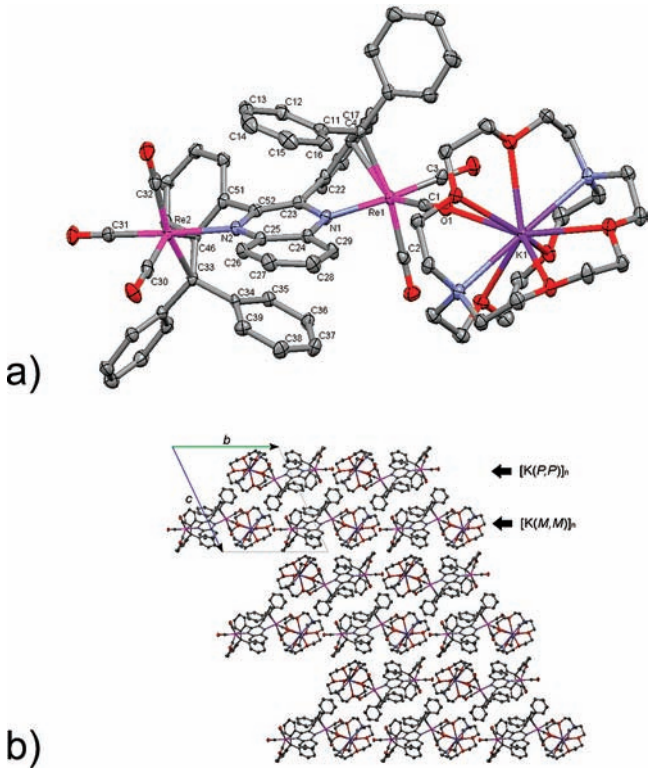

Figure 5. (a) CSD Mercury diagram of [K(222)][**3c**] drawn at the 30% probability level: atoms of hydrogen have been omitted for clarity. (b) Projection of the crystal lattice along the crystallographic *a* axis showing the stacking of homochiral sheets of (*P*,*P*)-[K(222)][**3c**] and (*M*,*M*)-[K(222)][**3c**]: atoms of hydrogen have been omitted for clarity.

Scheme 3

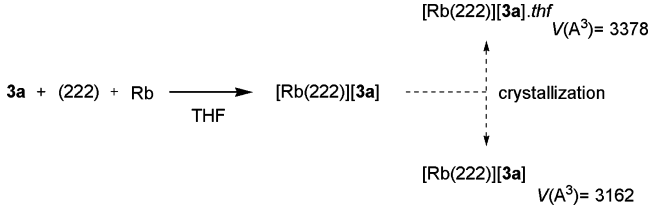

Using G03 and the B3LYP hybrid functional, 6-31G(d) and/or LANL2DZ basis sets were used to optimize the geometries of neutral and anionic complexes. Only manganese complexes could be optimized with the 6-31G(d) basis set, and attempts to reach convergence for **IIIc** and **IIIc**$^-$ failed probably owing to the large size of the structures. Nevertheless, full optimizations were achieved with LANL2DZ basis sets for both complexes.

Using ADF, all geometries were optimized using the Becke−Perdew functional (BVP86 also noted BP) with TZP basis sets for all atoms. Calculations were also carried out for **I** and **I**$^-$ for comparison. For both DFT methods, i.e., G03−B3LYP and ADF−BP (Table 6), optimized bond lengths matched satisfactorily with X-ray diffraction geometries, with the largest deviation of interatomic distances not exceeding 0.05 Å in all cases (cf. the Supporting Information). Even though it is notorious that G03−B3LYP with LANL2DZ basis sets yields systematically slightly longer bond lengths, the values computed with this DFT method reproduced quite well X-ray diffraction data too. The largest discrepancies for computations carried out with G03−B3LYP were, nonetheless, found for the average interplanar angle Π and distance *p* (Figure 10 and the Supporting Information), which amounted to ca. 13° and 0.4 Å, respectively. The ADF−BP/TZP-calculated geometry closely fitted crystallographic data. For convenience, only the results stemming from ADF−BP/TZP geometry optimizations will be discussed below.

The arrangement of the helical architecture of both complexes is correctly reproduced for the average interplanar distance *p* (3.376 vs 3.308 Å for **IIIa** and 3.453 vs 3.443 Å for **IIIc**) and the average interplanar angle Π (24.1° vs 21.4° for **IIIa** and 23.9° vs 25.1° for **IIIc**) with respect to experimental X-ray diffraction structural data. Particularly, the slight twist of the quinoxaline ligand phenyl rings (7° vs 6° for **IIIa** and 5.3° vs 4.8° for **IIIc**) follows the trend of experimental values. It is worth noting the 2−3% overestimate for metal−N bond lengths in **IIIa**. For **IIIc**, we note less than a 1% underestimate for the metal−N bond and a calculated bond length l_2 (Figure 10 and Table 6), rather consistent with a partial double-bond character. As expected, the coordination geometry around metal centers is that of a distorted octahedron, and related optimized geometrical parameters are rather similar for the two neutral complexes. In compliance with X-ray data, the main differences concern the coordination sphere around the metals, whereby bond lengths are significantly longer in **IIIc** than in **IIIa** (i.e., 2.188 vs 1.959 Å for Re−N vs Mn−N bond length). This reflects not only the difference in the covalent radii (r_{Mn} = 1.39 Å and r_{Re} = 1.51 Å[44]) but also a π-back-donation more significant for rhenium than for manganese. The ADF−BP molecular orbital diagrams of **IIIa** and **IIIc** are depicted in Figure 11, and their orbital compositions are given in Tables 7 and 8. Considering the anionic structures **IIIa**$^-$ and **IIIc**$^-$, no appreciable changes in the individual bond lengths and angles could be discerned. The most noteworthy deviations are noted for bond lengths within the quinoxaline core. Indeed, upon formal one-electron reduction of **IIIc** into **IIIc**$^-$, distance d_1 undergoes shortening while d_2, d_3, d_4 undergo elongation (Table 6). This trend is clearly confirmed by

(42) Frisch, M. J.; Trucks, G. W.; Schlegel, H. B.; Scuseria, G. E.; Robb, M. A.; Cheeseman, J. R.; Montgomery, J. J. A.; Vreven, T.; Kudin, K. N.; Burant, J. C.; Millam, J. M.; Iyengar, S. S.; Tomasi, J.; Barone, V.; Mennucci, B.; Cossi, M.; Scalmani, G.; Rega, N.; Petersson, G. A.; Nakatsuji, H.; Hada, M.; Ehara, M.; Toyota, K.; Fukuda, R.; Hasegawa, J.; Ishida, M.; Nakajima, T.; Honda, Y.; Kitao, O.; Nakai, H.; Klene, M.; Li, X.; Knox, J. E.; Hratchian, H. P.; Cross, J. B.; Bakken, V.; Adamo, C.; Jaramillo, J.; Gomperts, R.; Stratmann, R. E.; Yazyev, O.; Austin, A. J.; Cammi, R.; Pomelli, C.; Ochterski, J. W.; Ayala, P. Y.; Morokuma, K.; Voth, G. A.; Salvador, P.; Dannenberg, J. J.; Zakrzewski, V. G.; Dapprich, S.; Daniels, A. D.; Strain, M. C.; Farkas, O.; Malick, D. K.; Rabuck, A. D.; Raghavachari, K.; Foresman, J. B.; Ortiz, J. V.; Cui, Q.; Baboul, A. G.; Clifford, S.; Cioslowski, J.; Stefanov, B. B.; Liu, G.; Liashenko, A.; Piskorz, P.; Komaromi, I.; Martin, R. L.; Fox, D. J.; Keith, T.; Al-Laham, M. A.; Peng, C. Y.; Nanayakkara, A.; Challacombe, M.; Gill, P. M. W.; Johnson, B.; Chen, W.; Wong, M. W.; Gonzalez, C.; Pople, J. A. *Gaussian03*, revision *C.02*; Gaussian, Inc.: Wallingford, CT, 2004.

(43) *Amsterdam Density Functional*; ADF2003.01 ed.; Department of Theoretical Chemistry, Vrije Universiteit: Amsterdam, The Netherlands, 2003.

(44) Cordero, B.; Gomez, V.; Platero-Prats, A. E.; Reves, M.; Echeverría, J.; Cremades, E.; Barragan, F.; Alvarez, S. *Dalton Trans.* **2008**, 2832–2838.

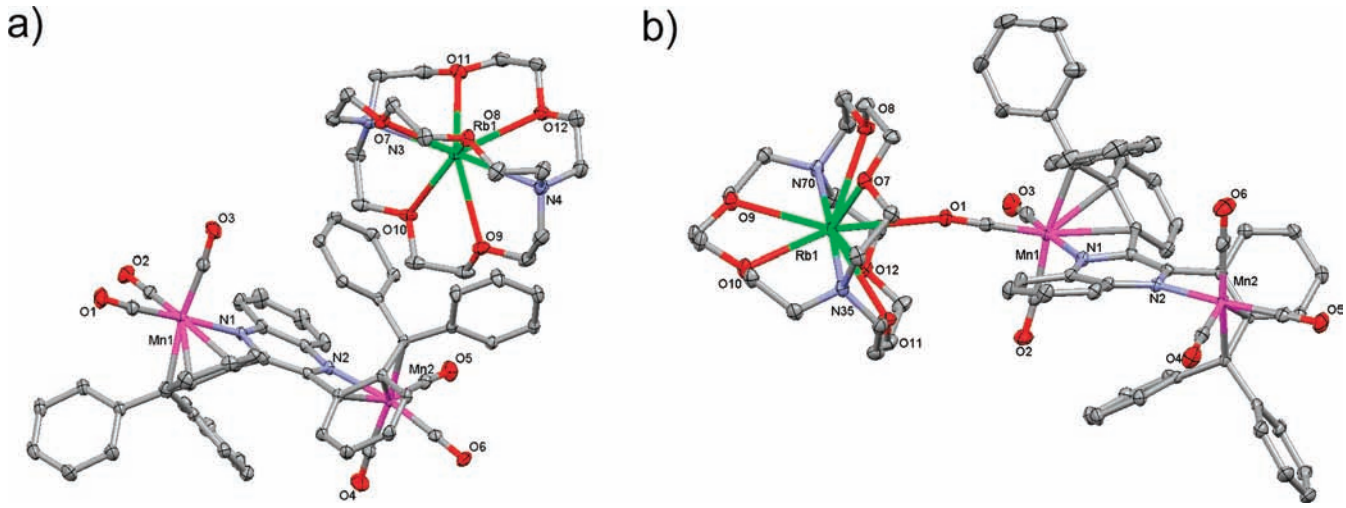

Figure 6. CSD Mercury views of the structure of [Rb(222)][**3a**]: (a) asymmetric unit of [Rb(222)]**3a**·THF; (b) asymmetric unit of [Rb(222)][**3a**].

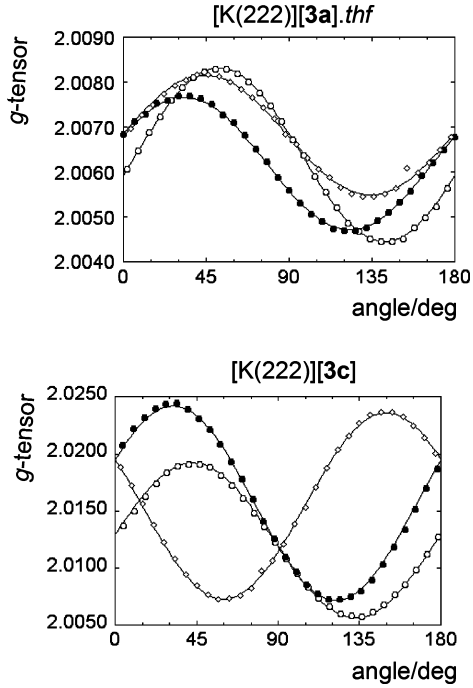

Figure 7. Angular dependence of the *g* factor within three orthogonal planes at room temperature for the crystals of [K(222)][**3a**]·THF and [K(222)][**3c**]. Lines are fits to the theoretical expression for the anisotropy of the *g* factor (g^2 is considered).

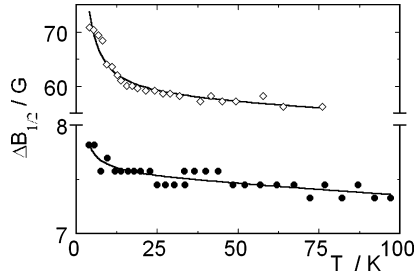

Figure 8. Temperature dependence of the full width at half-maximum of the EPR spectra of single crystals of [K(222][**3a**], lower curve, and [K(222][**3c**], upper curve. Lines are guides for the eyes.

crystallographic information available for **3a**, **3a**$^-$, **3c**, and **3c**$^-$, which indicate similar variations. It is worth noting that only the values of Δ_{a-n} (Table 6) related to d_5, l_2, m_2, and m_3 in [K(222)][**3a**]·THF and **3a** and those related to m_2 and m_3 in [K(222)][**3c**] and **3c** are in absolute value equal or higher than 3σ, whereby σ is the highest value of estimated standard deviation for corresponding interatomic distances in either neutral or anionic species. From this point of view, the variation $\Delta_{a-n}(m_2)$ upon one-electron reduction of either **3a** or **3c** accounts for a slight shift of the hapticity of the metal-bound benzyl moiety from a formal $\eta^2-\eta^1$ mode in the neutral form to $\eta^1-\eta^1$ in the reduced form, which is also well reproduced in the computed structures.

Although ligand **I** does not correspond to the residue that could result from the demetalation of either **3a** or **3c**, it provides a pertinent reference because of the π character of its frontier orbitals. The energy levels of ligand **I** are displayed in Figure 11. As compared to the quinoxalyl-centered LUMO of **I**, the quinoxalyl-centered LUMOs in **IIIa** and **IIIc** are stabilized by 0.226 and 0.336 eV, respectively. In addition, the substitution of the two manganese(I) centers in **IIIa** for two rhenium(I) centers in **IIIc** results in a narrowing of the HOMO−LUMO gap by 0.272 eV.

The close HOMO (MO 150) and HOMO−1 (MO 149) of **IIIa** possess a significant metal character (16% for MO 150 and 18% for MO 149). The next-lower-lying HOMOs 148 and 147 are significantly localized at the $Mn(CO)_3$ fragment. The LUMO, which lies way below the level of LUMO+1, mostly consists of the π^* orbital of the quinoxalyl moiety (72% in character). The energy level scheme for **IIIc** is similar to that of **IIIa** (Figure 11). Nevertheless, a slight shift to a higher energy is observed for HOMO and HOMO−1, which are less heavily weighted on the metal atom (5% for MO 158 and 7% for MO 157), with a shift to lower energies for MOs 153−156 also being noted. Another difference with **IIIa** can be outlined here, that is, the marked π^* quinoxalyl character of LUMO+1. In **IIIa**, this orbital consists of a more balanced combination of $Mn(CO)_3$ and quinoxalyl contributions. In anions **IIIa**$^-$ and **IIIc**$^-$, the compositions of HOMO and HOMO−1 are not significantly altered and remain slightly delocalized on the metal. The singly occupied molecular orbitals (SOMOs; Figure 12) are

Table 4. Experimental and Calculated Values of the Isotropic EPR Parameters (hfcc's in Gauss) for $\mathbf{1}^-$, $\mathbf{3a}^-$, and $\mathbf{3c}^-$ and Their Corresponding Gas-Phase Models $\mathbf{I}^-$, $\mathbf{IIIa}^-$, and $\mathbf{IIIc}^-$

	exptl hfcc						calcd hfcc (G03−B3LYP)					
							LANL2DZ		6-31G(d)		6-311+G(d)	6-311+G(2d)
compound	K[**1**]	[Rb(222)][**1**]	K[**3a**]	[K(222)][**3a**]	K[**3c**]	[K(222)][**3c**]	**IIIa**$^-$	**IIIc**$^-$	**I**$^-$	**IIIa**$^-$	**IIIa**$^-$	**IIIa**$^-$
^{55}Mn or ^{185,187} Re			4.60	4.54			0	0	0	0	−3.9	−3.8
^{14}N	5.2	5.1	6.10	6.42	5.60	5.35	8.7	8.9	4.4	6.5	4.6	4.8
$^{1}H_{6,7}$	1.9	1.45	1.60	1.66	2.00	2.40	−2	−1.7	−1.4	−1.4	−1.3	−1.4
$^{1}H_{5,8}$	1.7	2.38	1.30	1.44	1.50	1.42	−1.4	−1.4	−3	−1.9	−1.7	−1.8
$^{1}H_{ortho}$		0.42					−0.1	0	−0.5	0	0	0
$^{1}H_{meta}$		0.14					0.2	0	0.2	0	0	0
$^{1}H_{para}$		0.42					−0.4	−0.2	−0.6	−0.2	−0.2	−0.2
g_{iso}		2.0031	2.0035		2.0042							

Table 5. Experimental and Calculated Values of the Anisotropic Hyperfine Coupling Constants and **g** Tensors (in Gauss) for $\mathbf{1}^-$, $\mathbf{3a}^-$, and $\mathbf{3c}^-$ and Their Corresponding Gas-Phase Models $\mathbf{I}^-$, $\mathbf{IIIa}^-$, and $\mathbf{IIIc}^-$

	exptl hfcc			calcd hfcc (G03−B3LYP)					
				LANL2DZ		6-31G(d)		6-311+G(d)	6-311+G(2d)
	[Rb(222)][**1**] [a]	[K(222)][**3a**] [b]	[K(222)][**3c**] [b]	**IIIa** $^-$	**IIIc** $^-$	**I**$^-$	**IIIa** $^-$	**IIIa** $^-$	**IIIa** $^-$
^{55}Mn or ^{187,185}Re				−2.9	0.4		3.4	3.2	3.2
				−0.4	−0.1		−2.8	−2.7	−2.7
				3.2	−0.2		−0.6	−0.5	−0.5
^{14}N	9.0			10.0	10.2	9.3	9.5	10	10
	−7.0			−5.0	−5.0	−4.6	−4.7	−5	−5
	−7.0			−4.8	−5.2	−4.6	−4.9	−5.2	−5
g tensor	2.0035	2.0055	1.9996				1.999		
	2.0027	2.0043	2.0188				2.009		
	2.0009	2.0095	2.0249				2.000		

[a] Frozen solution. [b] Single crystal.

Table 6. Key Structural Parameters Defined in Figure 10 That Are Relevant to the Geometrical Changes Occurring upon Reduction of **3a**−**c** and **IIIa**−**c** (ADF−BP/TZP) into $\mathbf{3a}-\mathbf{c}^-$ and $\mathbf{IIIa}-\mathbf{c}^-$ (ADF−BP/TZP)

parameter	**3a**	[(222)K]**3a**·THF	Δ_{a-n} [d]	**3c**	[(222)K]**3c**	Δ_{a-n} [d]	**IIIa**	**IIIa**$^-$	Δ_{a-n} [d]	**IIIc**	**IIIc**$^-$	Δ_{a-n} [d]
Distances (Å)												
d_1 [a]	1.410(2)	1.377(2)	−0.033	1.412(10)	1.363(8)	−0.049	1.408	1.392	−0.016	1.421	1.392	−0.029
d_2 [a]	1.324(4)	1.3591(19)	+0.035	1.321(9)	1.371(8)	+0.050	1.339	1.328	−0.011	1.311	1.335	0.024
d_3 [a]	1.372(4)	1.381(2)	+0.009	1.370(8)	1.378(7)	+0.008	1.375	1.363	−0.012	1.350	1.361	0.011
d_4 [a]	1.409(2)	1.419(2)	+0.010	1.423(10)	1.428(8)	+0.005	1.413	1.405	−0.008	1.399	1.403	0.004
d_5 [a]	1.355(5)	1.389(3)	+0.034	1.374(11)	1.393(9)	+0.019	1.360	1.368	0.008	1.357	1.373	0.016
l_1 [a]	1.440(3)	1.434(2)	−0.006	1.440(10)	1.450(8)	+0.010	1.440	1.435	−0.005	1.448	1.447	−0.001
l_2 [a]	1.459(5)	1.473(2)	+0.014	1.476(10)	1.493(8)	+0.017	1.462	1.450	−0.012	1.453	1.454	0.001
m_1 [a]	2.0501(17)	2.0460(14)	−0.004	2.178(6)	2.147(6)	−0.031	1.959	2.018	0.059	2.188	2.187	−0.001
m_2 [a]	2.394(2)	2.3802(16)	−0.014	2.537(7)	2.589(6)	+0.052	2.393	2.358	−0.035	2.523	2.568	0.045
m_3 [a]	2.212(2)	2.2263(16)	+0.014	2.360(7)	2.377(6)	+0.017	2.158	2.153	−0.005	2.348	2.369	0.021
m_4 [a]	2.158(3)	2.1587(16)	+0.001	2.270(7)	2.269(6)	−0.001	2.099	2.104	0.005	2.309	2.301	−0.008
$\langle m_{CO} \rangle$ [b]	1.795(3)	1.7971(19)	+0.002	1.914(9)	1.918(8)	+0.004	1.718	1.710	−0.008	1.958	1.952	−0.006
p [c]	3.376	3.457	+0.081	3.453	3.430	−0.023	3.308	3.429	0.121	3.443	3.442	−0.001
Angles (deg)												
$\|\Psi\|$ [c]	8.5(3)	7.6(3)	−0.9	6.4(12)	9.6(9)	+3.2	9.6	7.4	−2.2	5.3	4.2	−1.1
θ [c]	106.5(2)	107.92(13)	+1.4	108.2(6)	107.3(4)	−0.9	109.6	107.3	−2.3	109.3	109	−0.3
Π [c]	24.07	25.82	+1.75	23.87	22.79	−1.08	21.44	27.31	5.87	25.12	26.3	1.18

[a] Average value for equivalent interatomic distances extracted from crystallographic data. [b] Average value for all metal-to-carbonyl carbon distances. [c] Average value extracted from crystallographic data. [d] Variation of the geometrical parameter upon conversion of the neutral species into its related radical anion.

identical with the corresponding LUMOs in the neutral species and are mainly located at the quinoxalyl moiety with negligible participation of the metal (ca. 2%) for $\mathbf{IIIc}^-$.

Atomic spin densities, which were also calculated to probe the delocalization of the added electron, are listed in Table 9. According to the latter, the single electron is located at the quinoxalyl moiety in both complexes, in agreement with a ligand-centered system. For both complexes, spin populations at metals are very weak if not negligible. Quite worth noting is the partially positive charge on rhenium atoms, whereas a negative charge is observed for manganese atoms for the neutral and anionic forms of the complexes (+1.26 for **IIIc** vs −0.44 for **IIIa** and +1.30 for $\mathbf{IIIc}^-$ vs −0.35 for $\mathbf{IIIa}^-$).

EPR Properties. The EPR parameters calculated with G03−B3LYP and different basis sets for each radical anion are reported in Tables 4 and 5. Values obtained with 6-311+G(d) and 6-311+G(2d,p) were computed on a single point of optimized geometries with B3LYP/6-31G(d). Each different basis set reproduces the experimental trends for $\mathbf{IIIa}^-$ and $\mathbf{I}^-$. Considering only isotropic couplings computed

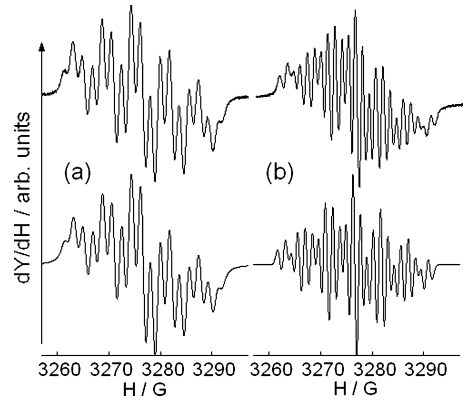

Figure 9. Experimental (upper trace) and simulated (lower trace) EPR spectrum of the radical anion of (a) K[**3c**] in fluid solution (THF) at room temperature and (b) [K(222)][**3c**] in fluid solution (THF) at room temperature. Parameters for the simulations are given in Table 4.

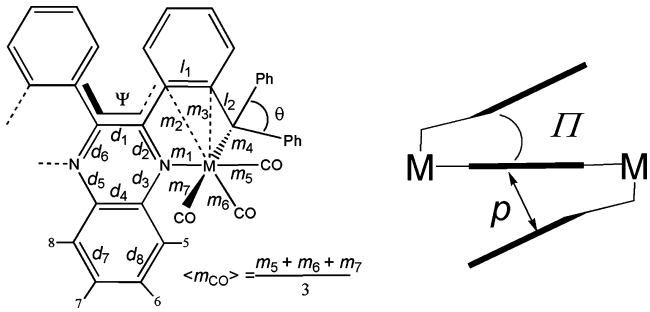

Figure 10. Description and definition of the structural parameters taken into account to compare the structural changes occurring upon the one-electron reduction of **3a**−**c**/**IIIa**−**c** into **3a**−**c**$^-$/**IIIa**−**c**$^-$. Parameter Π corresponds to the averaged interplanar angle between a phenyl fragment and the quinoxalyl core. Parameter p is the averaged interannular distance between the centroids of the phenyl ring and the pyrazino fragment of the quinoxalyl core.

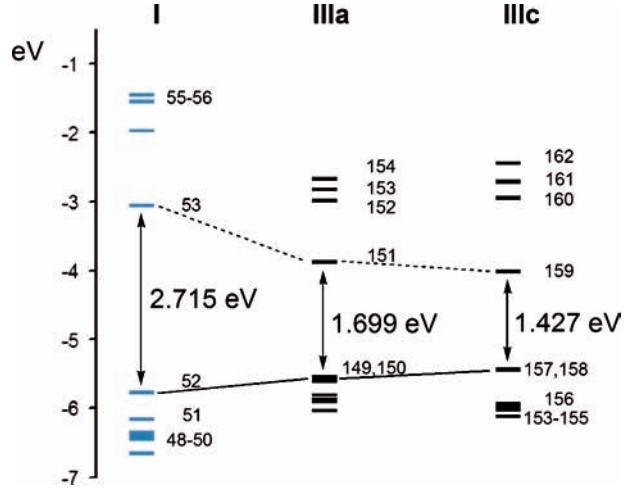

Figure 11. Molecular orbital diagrams of neutral compounds, **I**, **IIIa**, and **IIIc**, i.e., the computed models (ADF−BP/TZP) of **1**, **3a**, and **3c**, respectively: the dashed line links the levels corresponding to the LUMOs of each species, whereas the solid line links the HOMOs of each species.

with various basis sets leads to the conclusion that the addition of diffuse and polarization functions, which better describe the spatial extension of the electron added in the reduction process, gives reliable values for **IIIa**$^-$. A comparison with the values computed using the pseudopotential LANL2DZ basis set shows a satisfactory match to the experimental values, in agreement with a similar trend reported elsewhere for small transition-metal complexes.[45] The most significant deviation of ca. 30% is found for the isotropic coupling of ^{14}N (8.7 vs 6.1 G). Because manganese inner electrons are described by an effective core potential (ECP), this basis set is not suitable for the calculation of the Fermi contact term. Thus, as described above, the LANL2DZ basis appears to provide a good estimation of the geometry and some confidence in the reliability of calculated coupling constants of **IIIc**$^-$. Indeed, values are close to the experimental values obtained for **3c**$^-$, with the same gap for the isotropic coupling of ^{14}N being reproduced. Another noticeable result in Table 5 is that the calculated values for the anisotropic coupling constants, which are too far from the experimental values for the three anionic species, are insensitive to the basis set. These values are identical with those of **IIIa**$^-$ and **IIIc**$^-$. The SOMO of **IIIc**$^-$ (Figure 12) is in agreement with an elongation of d_2, d_3, and d_5 and a shortening of d_1 bond lengths (see the notations in Figure 10). As shown by the molecular orbital energy diagram, the lower-lying LUMO π^* of neutral forms of complexes gets lower in energy compared to that of **I** and behaves as an electron reservoir by stabilizing electrons in excess around the metal. This and the decrease of the HOMO−LUMO gap has to be correlated with the more accessible reduced state, as given by the reduction potentials in electrochemistry.

With respect to spin, the minor role of the metal nuclei upon charge addition is remarkable. Indeed, small or vanishing isotropic hfcc's are assessed for the metal centers ($a^{185,187}_{Re} = 0$ vs $a^{55}_{Mn} = 4.6$ G). This is quite unusual for a rhenium derivative, as compared to other known rhenium complexes of α-diimine ligands. As mentioned in the Introduction, EPR spectroscopy and DFT calculations have been previously shown to assist one another when discussing the electronic structure of $Re(CO)_3X$-based α-diimine derivatives. The observation of a g factor in fluid solution close to the free electron value ($g_e = 2.0023$) while dealing with heavy transition-metal ions with large spin−orbit interaction has been considered as possibly resulting from compensation effects,[46] so that a g factor close to g_e does not necessarily imply the vanishing spin density at the metal center. For $Re(CO)_3$ halide-based α-diimine derivatives, most of the shift of the g factor has been attributed to the spin−orbit coupling from the metal center and to a Re^I d_π−π^*(ligand) orbital mixing. The latter contribution is affected by the electronegativity of the spin-bearing diimine ligand and by the possible competing ligands around the metal center.[34,37] In the present study, experimental anisotropic hfcc's are available only for the quinoxaline ligand and the spectrum was easily simulated by assuming two ^{14}N hyperfine axial tensors with parallel principal axes. The observed value of ^{14}N $\tau_{||}$ leads to a spin density of 0.39 in the p_π orbital of each nitrogen atom.[47] The computed values are quite identical with the experimental ones, and they have similar values for each anionic complex. ^{14}N hfcc's are also close to the values reported for

(45) Pietrzyk, P.; Piskorz, W.; Sojka, Z.; Broclawik, E. *J. Phys. Chem. B* **2003**, *107*, 6105–6113.
(46) Kaim, W.; Kohlmann, S. *Inorg. Chem.* **1990**, *29*, 2909–2914.

Table 7. ADF−BP/TZP-Calculated Energies and Percentage Composition of Selected Frontier Molecular Orbitals in **IIIa**

MO	*E* (eV)	Mn (%)	quinoxalyl (%)	CO (%)	character
Unoccupied					
154	−2.667	8 (d_{xy}); 7 (p_y); 4 (d_{yz}); 4 ($d_{x^2-y^2}$); 5 (d_{z^2})	0	12	d
153		1 (d_{yz})	38	0	π^* quinox
152		9 (d_{xy}); 7 (p_y); 4 (d_{z^2}); 4 ($d_{x^2-y^2}$); 1 (d_{z^2})	7	10	d + CO
151	−3.877	1 (d_{xy}); 1 (d_{xz})	72	0	π^* quinox
Occupied					
150	−5.546	10 (d_{z^2}); 2 ($d_{x^2-y^2}$); 2 (d_{xy}); 1 (p_z); 1 (p_x)	0	3	d
149	−5.612	9 (d_z^2); 5 (d_{xy}); 2 (p_z); 2 (d_{yz})	0	2	d
148	−5.802	23 (d_{xy}); 14 (d_{z^2}); 14 (d_{yz}); 6 (d_{xz})	0	13	d + CO
147	−5.870	19 (d_{yz}); 7 (d_{xy}); 4 (d_{xz}); 2 ($d_{x^2-y^2}$)	1	7	d

Table 8. ADF-BP/TZP Calculated Energies and Percentage Composition of Selected Frontier Molecular Orbitals in **IIIc**

MO	*E* (eV)	Re (%)	quinoxalyl (%)	CO (%)	character
Unoccupied					
162	−2.244	9 (p_y); 5 (d_{xy}); 4 (d_{z^2}); 2 ($d_{x^2-y^2}$); 2 (d_{yz}); 2 (p_x); 2 (p_z)	2	25	d + CO
161		8 (p_y); 4 (d_{z^2}); 5 (d_{xy}); 2 ($d_{x^2-y^2}$); 2 (p_x); 2 (d_{yz})	0	9	d + CO
160	−2.949	0	56	0	π^* quinox
159	−4.009	0	77	0	π^* quinox
Occupied					
158	−5.436	5 (d_z^2)	0	3	d
157	−5.447	4 (d_z^2); 2 (d_{xy}); 1 (p_z)	0	3	d
156	−5.947	6 (d_{xy}); 17 (d_{yz})	0	8	d + CO
155	−5.986	13 (d_{yz}); 8 (d_{xy}); 4 (d_{xz}); 2 (d_{z^2})	0	5	d

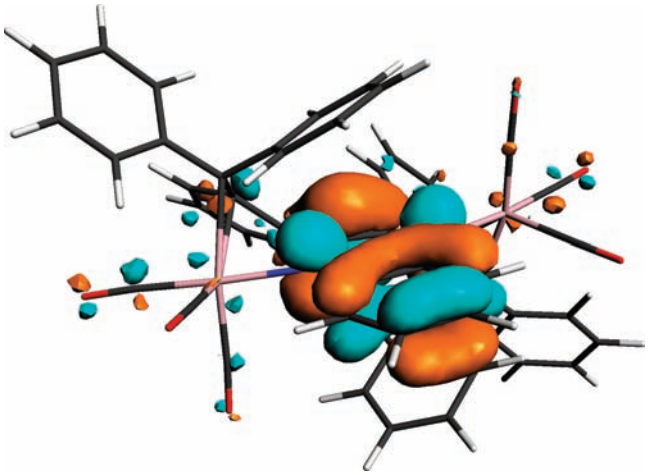

Figure 12. ADF-view drawing of the Kohn−Sham singly occupied molecular orbital (SOMO) of **IIIc**$^-$. Color scheme for the atoms: red, oxygen; pink, rhenium; blue, nitrogen (occulted); dark gray, carbon; white, hydrogen.

α-diimine derivatives, ca. 5 G. Nevertheless, the presence of heavy rhenium(I) and manganese(I) centers probably broadens lines, hence preventing an assessment of hfcc's of nitrogen atoms within complexes. The fact that the odd electron is located at the central ligand, i.e., the quinoxalyl core, is confirmed by the small experimental isotropic *g* values in both cases (2.0035 for **IIIa**$^-$ vs 2.0042 for **IIIc**$^-$; Table 5). Given the large difference between spin−orbit coupling constants of rhenium and manganese (2285 cm^{-1} for ^{185,187}Re vs 239 cm^{-1} for ^{55}Mn),[48] it was expected to observe (i) a shift of the *g* factor with respect to g_e and (ii) a larger shift of the *g* factor for **IIIc**$^-$ than for **IIIa**$^-$. The observed weak effects are clearly corroborated by the main

Table 9. Summed Mulliken Charges (q_a) and Spin Populations (ADF−BP/TZP) at the Metal Centers and at the Quinoxalyl Core

	q_a				spin population	
atoms	**IIIa**	**IIIa**$^-$	**IIIc**	**IIIc**$^-$	**IIIa**$^-$	**IIIc**$^-$
∑Mn or ∑Re	−0.44	−0.35	1.26	1.30	0.061	0.024
$\sum N_{quinox}$	−0.52	−0.63	−0.80	−0.93	0.391	0.399
$\sum C_{quinox}$	1.53	1.37	1.56	1.05	0.375	0.402

results of the DFT calculations presented here. Therefore, the situation found here is typical of a ligand-centered organic radical with a weak if not negligible contribution of the metal center to the spin density.

Conclusion

The influence of the nature of the metal on the bonding and properties of two triple-decker complexes containing an encapsulated quinoxaline core has been investigated. A new rhenium complex has been synthesized, and its chemical and spectroscopic properties were compared to that of the manganese analog in the reduced state. The structures of four unprecedented paramagnetic metalloorganic salts have been resolved by X-ray diffraction analyses. According to the latter, the bonding and overall geometry of the neutral species are relatively similar to those of the related paramagnetic salts apart from slight changes of hapticity of the metal-bound benzyl fragments and sensible intraannular distortions of the quinoxalyl fragment, upon reduction. In either the neutral or reduced state, replacement of the manganese(I) center by the more electronegative rhenium(I) center does not affect drastically the bonding around the coordinated d^6 metal center. The only noticeable differences are the interatomic distances in the metal's coordination sphere, which are longer, as expected, in the rhenium complexes by about 0.1 Å as compared to the manganese isomers. All of these features are reasonably reproduced by our computations. Despite apparent similarities between the molecular

(47) Morton, J. R.; Preston, K. F. *J. Magn. Reson.* **1978**, *30*, 577–582.
(48) Goodman, B. A.; Raynor, J. B. *Adv. Inorg. Chem. Radiochem.* **1970**, *13*, 135–362.

orbitals of **IIIa** and **IIIc**, the HOMO−LUMO gap is significantly larger for the manganese complex as compared to the rhenium counterpart. The red shift observed for the electronic MLCT transition detected in UV−visible and the relative position of the electrochemical reduction potential are consistent with these observations. The observed almost identical behavior of both complexes upon reduction is consistent with a quinoxalyl-centered LUMO in the neutral species **3a** and **3c**. With respect to radical anions, all of the experimental and theoretical results account for a fully ligand-centered electron. When $\mathbf{1}^-/\mathbf{I}^-$ is compared to the complexes, this spin/charge location was probed in the anions by EPR in fluid and frozen solutions through the average g value close to the free electron g_e value and hfcc's mostly related to the quinoxalyl moiety. Moreover, the reduced state is more accessible in the complexes than in **1/I**. The presence of the metal stabilizes the radical anion, although the charge is not concerned with the metal. These experimental findings are corroborated by the computed molecular orbital energy diagrams of the species addressed here, which show a strong decrease of the HOMO−LUMO gap by around 1 eV upon "metalation", while keeping the spin population over the ligand. The salts synthesized in this study proved to be persistent for weeks in solution as well as in the crystal state, under anhydrous and anaerobic conditions. It is inferred from this study that the chelation of the transition-metal centers combined with the encapsulation of the central quinoxalyl core contribute greatly to the observed long-lived character of the radical-anionic species reported here and which, to the best of our knowledge, is unprecedented for metalloorganic radical anions.

Experimental Section

General Considerations. All experiments were carried out under a dry atmosphere of argon with dry and degassed solvents. Radical anions were prepared in a Vac Atmospheres glovebox filled with nitrogen gas. Cryptand 222 was purchased from Aldrich (4,7,13,16,21,24-hexaoxa-1,10-diazabicyclo[8.8.8]hexacosane, Kryptofix 222) and used without further purification. 1,1-Diphenyldiazomethane was prepared by oxidation of commercially available benzophenone hydrazone over yellow HgO in dry toluene. Complex **3a** was prepared by following a published procedure, and compound **1** was purchased from Aldrich and used without further purification.[31] NMR spectra (^{13}C and ^{1}H nuclei) were acquired with a Bruker Avance 500 spectrometer at 263 K unless otherwise stated. Chemical shifts are reported in parts per million downfield of Me_4Si, and coupling constants are expressed in hertz. IR spectra were measured with a Perkin-Elmer FT spectrometer. Elemental analyses (reported in percent mass) were performed at Institut Charles Sadron, Strasbourg, France. High-resolution electrospray mass spectrometry (HRESMS) experiments were carried out in the negative-polarity mode with a MicroTOF Bruker spectrometer. Chromatographic separations were performed at subambient temperatures with a Merck Geduran silica (Si 60, 40−60 μm) in columns packed in dry *n*-pentane with a maximum positive argon pressure of 0.4 bar. UV−visible spectra were performed with a Uvikon Bio-Tek Instruments spectrometer at ambient temperature in 1 cm optical path quartz cells with distilled dry solvents. Wavelengths λ are expressed in nanometers, and extinction coefficients ϵ are expressed in liters per centimeters per mole.

Solution EPR Experiments. EPR spectra were recorded with an ESP 300E spectrometer (Bruker) operating at X band and equipped with a standard TE102 rectangular cavity. Computer simulations of the EPR spectra were performed with the help of *Simfonia* (Bruker) and *Winsim* (NIEH Public Software) softwares. Radical anions were generated by chemical reduction on a potassium mirror with distilled solvent under an argon atmosphere or by electrolysis in a microcell set up in a 5 mm inner diameter quartz tube. Electrolyses were performed at a controlled potential with a three-electrode configuration under an atmosphere of argon using a platinum wire as the working electrode, a platinum wire as the auxiliary electrode, and a silver wire as the pseudoreference electrode. A dilute solution (ca. 3×10^{-3} M) of the precursor neutral complex was prepared with $TPAPF_6$ (10^{-1} M) as the supporting electrolyte.

EPR Experiments with Single Crystals. Single crystals were transferred from the X-ray diffractometer to a glovebox, where they were fixed to a cubical Teflon sample holder, the shape of which allows successive rotations within three orthogonal planes. The Teflon sample holder was carefully placed within a 5 mm diameter EPR sample tube, which was sealed under nitrogen and placed in the EPR spectrometer's cavity. Sample tube rotation was computer-controlled by means of a step motor, and data acquisition was automated. The elements of the squared **g** tensor were determined by fitting the data to the following equation:

$$g_{\mathrm{exp}}{}^2(\theta) = g_{ii}{}^2 \sin^2\theta + 2g_{ij}{}^2 \sin\theta\cos\theta + g_{jj}{}^2 \cos^2\theta$$

with (i, j) indices running over three orthogonal directions (x, y, z).

In this equation, θ is the angle between the static field and the laboratory frame attached to the rotating crystal. Once the required six elements of the symmetrical squared **g** tensor were determined, the principal axes of the **g** tensor were obtained through a diagonalization procedure.

Electrochemical Experiments. All measurements were made at room temperature, under an atmosphere of dry argon with an Eco Chemie (Autobab model PGSTAT 30) potentiostat computer-controlled with the *GPSE* software (version 4.9). Tetra-*n*-butylammonium hexafluorophosphate was used as the electrolyte in solution in dry solvents saturated with argon (0.1 M, CH_3CN, CH_2Cl_2). Cyclic voltammetry experiments were carried out using an undivided cell comprising a three-electrode system: a platinum disk working electrode (2 mm diameter), a platinum wire of 1 mm diameter as the counter electrode, and, because of the sensitivity of the reduced species to water, a silver wire of 1 mm diameter as the pseudoreference electrode. All potentials were referenced against the ferrocenium−ferrocene (Fc^+/Fc) couple and subsequently extrapolated against a standard SCE.

Spectroelectrochemical Measurements. Spectroelectrochemical measurements were performed in a thin-layer cell (0.1 mm) through an OTTLE made of a platinum minigrid (1000 mesh). The auxiliary electrode was a platinum wire, and a Ag/AgCl electrode was used as the reference. Tetra-*n*-butylammonium hexafluorophosphate was used as the electrolyte in solution in dry methylene chloride saturated with argon (0.1 M). The OTTLE cell was placed in an HP 8453 diode-array UV−visible spectrophotometer.

Experimental Procedure for the X-ray Diffraction Analysis of Compounds 2b, 3b, 3c, [K(222)][3a], [K(222)][3c], and [Rb(222)][3a]. Acquisition and processing parameters are displayed in Table 1. Reflections were collected with a Nonius Kappa CCD

diffractometer using Mo Kα graphite-monochromated radiation (λ = 0.710 73 Å).

Computational Details. Ground-state electronic structures have been calculated by DFT methods using Amsterdam Density Functional (ADF2003.01)[43] and *Gaussian 03*[42] software packages. Calculations for all species were done without any constrained symmetry. Within *Gaussian 03*, B3LYP[49,50] hybrid functionals and the 6-31G(d) basis set[51] for hydrogen, carbon, oxygen, nitrogen, and manganese atoms were used for neutral and anionic species. Calculations were also performed by using the ECP basis set on all atoms including rhenium species. The xenon core electrons were replaced by an ECP, and the DZ-quality Hay and Wadt Los Alamos ECP basis set (LANL2DZ)[52] was used for the valence electrons. With the ADF program, electron correlation was treated within the local density approximation in the Vosko−Wilk−Nusair parametrization.[53] Electronic configurations of atoms were described by a triple-ζ Slater-type orbital (STO) basis set for H 1s, C 2s and 2p, N 2s and 2p, and O 2s and 2p, augmented with a 3d single-ζ polarization for nitrogen, oxygen, and carbon atoms and with a 2p single-ζ polarization for hydrogen. A triple-ζ STO basis set was used for Mn 3d and 4s and Re 5d and 6s augmented with a 4p single-ζ polarization function for manganese and a 6p single-ζ polarization function for rhenium. The inner shells were treated with the frozen-core approximation. EPR properties were calculated on a single point of the optimized structure 6-31 G(d) for the *Gaussian 03* package. Representations of the molecular structures and orbitals were made using ADF-view v06.[54]

Synthesis of [2,3-(Diphenyl-$\kappa C^{2'},\kappa C^{2''}$]quinoxaline-$\kappa N^1,\kappa N^2$)-bis[tetracarbonylrhenium(I)] (2b). A solution of 2,3-diphenylquinoxaline **1** (0.68 g, 2.41 mmol) and (η^1-$PhCH_2$)$Re(CO)_5$[55] (4 g, 7.19 mmol) in toluene (20 mL) was brought to reflux and stirred for 24 h. The color of the medium quickly changed from pale yellow to deep red. The resulting solution was refluxed for up to 10 h and subsequently cooled to room temperature. Solvent was evaporated under reduced pressure, and the crude solid mixture was dissolved in CH_2Cl_2. Silica gel was added to the resulting solution, and the solvent was evacuated under vacuum. The resulting coated silica gel was loaded at the top of a SiO_2 column packed in dry *n*-pentane. A deep-red band containing compound **2b** was eluted with a 3:7 mixture of dichloromethane and pentane. Removal of the solvents under reduced pressure yields a red powder (1.336 g, 63%), which was recrystallized from a mixture of dichloromethane and *n*-pentane. Compound **2b**. Anal. Calcd for $C_{28}H_{12}N_2Re_2O_8$: C, 38.27; H, 1.38; N, 3.19. Found: C, 38.58; H, 1.76; N, 3.09. IR (CH_2Cl_2): ν(CO) 2091(m), 1997(s), 1978(s), 1935(s) cm^{-1}. ^1H NMR ($CDCl_3$, 273 K): δ 8.48 (m, 2H, $H_{quinoxalyl}$), 8.14 (dd, 2H, ^3J = 7.3 Hz, ^4J = 0.9 Hz, $H_{m\text{-phenylene}}$), 7.92 (d, 2H, ^3J = 8.0 Hz, $H_{p\text{-phenylene}}$), 7.84 (m, 2H, $H_{quinoxalyl}$), 7.22 (td, 2H, ^3J = 7.3 Hz, ^4J = 0.9 Hz, $H_{m\text{-phenylene}}$), 6.99 (ddd, 2H, ^3J = 8.5 Hz, ^4J = 7.3 Hz, ^5J = 1.3 Hz, $H_{o\text{-phenylene}}$). ^{13}C NMR ($CDCl_3$, 273 K): δ 191.5 (CO), 191.4 (CO), 187.7 (CO), 186.7 (CO), 169.5, 165.9, 150.3, 142.3, 140.0, 132.0, 131.4, 131.2, 129.4, 123.2. UV−visible λ_{max} (ϵ) (CH_2Cl_2): 319 (1.21 × 10^4), 352 (1.17 × 10^4), 379 (1.18 × 10^4), 418 (8.0 × 10^3), 480 (4.7 × 10^3), 517 (3.0 × 10^3).

Synthesis of {2,3-Bis[1′2′7′:η-2′-(diphenylmethylene)phenyl]quinoxaline-$\kappa N^1,\kappa N^2$}bis[tricarbonylrhenium(I)] (3c). A solution of diphenyldiazomethane (3.24 g, 16.7 mmol) in toluene (20 mL) was added to a boiling solution of compound **2b** (710 mg, 0.835 mmol) in toluene (15 mL) within 1 h. The color of the medium quickly changed from deep purple to brown. The solution was further stirred for 1 h and subsequently cooled to room temperature. The solvent was evaporated under reduced pressure, and the crude residue was dissolved in CH_2Cl_2. Silica gel was added to the resulting brown solution and the solvent evaporated subsequently. The coated silica gel was loaded at the top of a SiO_2 column packed in *n*-pentane. The first band containing the product **3b** was eluted with a 3:7 mixture of CH_2Cl_2 and *n*-pentane, and the second band containing the product **3c** was eluted with a 4:6 mixture of CH_2Cl_2 and pentane. Evaporation of the solvents afforded **3b** as a brown powder (405 mg, 48%) and **3c** as a dark-brown powder (290 mg, 29%). These two compounds are soluble in almost any organic solvent. Crystals of compound **3b** suitable for X-ray diffraction were obtained at −20 °C by the slow diffusion of *n*-heptane in a solution of compound **3b** in CH_2Cl_2, and crystals of compound **3c** were obtained at room temperature by the slow diffusion of *n*-heptane in a solution of compound **3c** in 1,2-dimethoxyethane. Compound **3b**. Anal. Calcd for $C_{39}H_{22}N_2Re_2O_7$: C, 46.61; H, 2.21; N, 2.79. Found: C, 46.65; H, 2.29; N, 2.60. IR (CH_2Cl_2): ν(CO) 2013 (m), 1996 (s), 1979 (s), 1929 (s), 1902 (s) cm^{-1}. ^1H NMR (CD_2Cl_2, 263 K): δ 8.30 (m, 1H, $H_{quinoxalyl}$), 8.12 (ddd, 1H, ^3J = 7.3 Hz, ^4J = 1.3 Hz, ^5J = 0.4 Hz, $H_{m\text{-phenylene}}$), 7.95 (m, 1H, $H_{quinoxalyl}$), 7.85 (m, 2H, $H_{quinoxalyl}$), 7.71 (broad d, 2H, ^3J = 6.6 Hz, $H_{o\text{-Ph,exo}}$), 7.57 (dd, 1H, ^3J = 8.4 Hz, ^4J = 0.9 Hz, $H_{m\text{-phenylene}}$), 7.46 (ddd, 1H, ^3J = 8.9 Hz, ^3J = 6.8 Hz, ^4J = 1.4 Hz, $H_{p\text{-phenylene}}$), 7.41−7.35 (m, 3H, $H_{m\text{-Ph,exo}}$ + $H_{m\text{-phenylene}}$), 7.27−7.18 (m, 3H, $H_{p\text{-Ph,exo}}$ + $H_{o\text{-phenylene}}$), 7.00−6.93 (m, 2H, $H_{o\text{-Ph,endo}}$ + $H_{m\text{-phenylene}}$), 6.76 (d, 1H, ^3J = 8.1 Hz, $H_{p\text{-phenylene}}$), 6.66 (m, 1H, $H_{o\text{-Ph,endo}}$), 6.18 (td, 1H, ^3J = 7.5 Hz, ^4J = 1.5 Hz, $H_{m\text{-Ph,endo}}$), 6.12 (tt, 1H, ^3J = 7.4 Hz, ^4J = 1.3 Hz, $H_{p\text{-Ph,endo}}$), 6.00 (tdd, 1H, ^3J = 7.5 Hz, ^4J = 1.5 Hz, ^5J = 0.4 Hz, $H_{m\text{-Ph,endo}}$). ^{13}C NMR (CD_2Cl_2, 263 K): δ 199.3 (CO), 196.9 (CO), 194.7 (CO), 192.5 (CO), 191.6 (CO), 188.1 (CO), 187.0 (CO), 171.2, 163.1, 152.3, 146.2, 146.0, 145.9, 143.7, 142.6, 141.9, 136.7, 135.1, 134.9 (2C), 134.8, 133.6 (2C), 131.7, 131.6, 131.4, 131.1, 130.6, 129.1, 128.4, 128.3, 128.1, 127.4, 126.6, 126.1, 125.9, 125.8, 124.4, 124.0, 123.8, 120.0, 87.8. UV−visible λ_{max} (ϵ) (CH_2Cl_2): 339 (9.1 × 10^3), 394 (8.1 × 10^3), 415 (7.8 × 10^3), 503 (3.7 × 10^3). Compound **3c**. Anal. Calcd for $C_{52}H_{32}N_2Re_2O_6$: C, 54.07; H, 2.79; N, 2.43. Found: C, 54.12; H, 2.84; N, 2.40. IR (*n*-heptane): ν(CO) 2000 (m), 1940 (s), 1912 (s) cm^{-1}. MS (ES^-). Calcd for $C_{52}H_{32}N_2Re_2O_6$: 1154.1376. Found: 1154.1448. ^1H NMR (CD_2Cl_2, 263 K): δ 7.76 (m, 2H, $H_{quinoxalyl}$), 7.77−7.50 (broad m, 4H, $H_{o\text{-Ph,exo}}$), 7.52 (m, 2H, $H_{quinoxalyl}$), 7.41−7.32 (broad m, 6H, $H_{m\text{-Ph,exo}}$ + $H_{m\text{-phenylene}}$), 7.25 (broad m, 4H, $H_{m\text{-phenylene}}$ + $H_{p\text{-phenylene}}$), 7.21 (tt, 2H, ^3J = 7.4 Hz, ^4J = 1.2 Hz, $H_{p\text{-Ph,exo}}$), 7.15 (dd, 1H, ^3J = 6.7 Hz, ^4J = 0.9 Hz, $H_{o\text{-phenylene}}$), 7.13 (dd, 1H, ^3J = 6.8 Hz, ^4J = 1.1 Hz, $H_{o\text{-phenylene}}$), 6.87−6.77 (m, 6H, $H_{m\text{-Ph,endo}}$ + $H_{o\text{-Ph,endo}}$), 6.33 (tt, 2H, ^3J = 7.3 Hz, ^4J = 1.3 Hz, $H_{p\text{-Ph,endo}}$), 6.13 (td, 2H, ^3J = 7.7 Hz, ^4J = 1.1 Hz, $H_{m\text{-Ph,endo}}$). ^{13}C NMR (CD_2Cl_2, 263 K): δ 199.2 (CO), 198.6 (CO), 194.8 (CO), 150.3, 146.7, 138.5, 135.3 (2C), 134.3, 133.8, 133.7, 133.1, 132.8, 129.5 (2C), 128.1, 128.0, 127.6, 126.9, 126.4, 125.3, 124.9, 120.0, 87.6. UV−visible λ_{max} (ϵ) (CH_2Cl_2): 315 (1.5 × 10^4), 373 (8.2 × 10^3), 402 (5.4 × 10^3), 470 (5.3 × 10^3), 518 (4.6 × 10^3).

Synthesis of 3c from 3b. A solution of diphenyldiazomethane (680 mg, 3.5 mmol) in toluene (10 mL) was added to a boiling

(49) Becke, A. D. *J. Chem. Phys.* **1993**, *98*, 5648–5652.
(50) Lee, C.; Yang, W.; Parr, R. G. *Phys. Rev. B* **1988**, *37*, 785–789.
(51) Hehre, W. J.; Ditchfield, R.; Pople, J. A. *J. Chem. Phys.* **1972**, *56*, 2257–2261.
(52) Hay, P. J.; Wadt, W. R. *J. Chem. Phys.* **1985**, *82*, 299–310.
(53) Vosko, S. D.; Wilk, L.; Nusair, M. *Can. J. Chem.* **1990**, *58*, 1200–1211.
(54) *Amsterdam Density Functional viewer*; ADFview 2006.01 ed.; Department of Theoretical Chemistry, Vrije Universiteit: Amsterdam, The Netherlands, 2006.
(55) Djukic, J.-P.; Doetz, K. H.; Pfeffer, M.; de Cian, A.; Fischer, J. *Inorg. Chem.* **1998**, *37*, 3649–3651.
(56) Edelmann, M. J.; Raimundo, J. M.; Utesch, N. F.; Diederich, F.; Boudon, C.; Gisselbrecht, J. P.; Gross, M. *Helv. Chim. Acta* **2002**, *85*, 2195–2213.

solution of compound **3b** (352 mg, 0.35 mmol) in toluene (10 mL) within 1 h. The solution was further stirred for 1 h and subsequently cooled to room temperature. The solvent was evaporated under reduced pressure, and the crude residue was dissolved in CH_2Cl_2. Silica gel was added to the resulting dark-brown solution and the solvent evaporated subsequently. The coated silica gel was loaded at the top of a SiO_2 column packed in pentane. A first minor brown band containing the unreacted substrate was eluted with a 3:7 mixture of dichloromethane and *n*-pentane, and a second dark-brown band containing **3c** was eluted with a 4:6 mixture of dichloromethane and *n*-pentane. Evaporation of the solvents afforded pure compound **3c** (288 mg, 72%).

General Procedure for the Crystallization of Radical Anions. A mixture of compounds **3a** or **3c** and cryptand 222 (1.5 equiv) dissolved in dry THF (ca. 2−3 mL) was reacted over a potassium mirror—or a rubidium droplet—in a glovebox filled with nitrogen gas. The color of the solution slowly turned from deep blue to dark red with compound **3a**, whereas no sensible change in color was observed with compound **3c**. The resulting solution was then transferred into a glass tube, and dry *n*-pentane was carefully added so as to form a limpid supernatant layer. Air-stable crystals of [M(222)][**3a**] (M = K, Rb) and [K(222)][**3c**] were obtained upon slow diffusion of the THF solution into *n*-pentane at room temperature after 1 week at 25 °C. Crystallographic data and experimental parameters are given in Table 1. Radical anion $\mathbf{3c}^-$ was analyzed by high-resolution electrospray mass spectrometry (negative mode) by direct injection. HRMS (ESI^-). Calcd for $C_{52}H_{32}N_2O_6Re_2$: 1154.1376. Found: 1154.1448. Electrospray mass spectrometry experiments carried with $\mathbf{3a}^-$ provided results identical with those reported previously.[34]

Acknowledgment. The National Centre for Scientific Research (CNRS) and the Department of Education and Research are gratefully acknowledged for their support. The authors thank Jean-Marie Mouesca (DRF-CEA, Grenoble, France) for helpful discussions and Michelle Lefèvre (IUT Robert Schuman) for proofreading of this Article.

Supporting Information Available: (1) Short description of the structures of **2b** and **3b**, (2) ESMS data for $\mathbf{3c}^-$, (3) spectroelectrochemical record for the reduction of **3a**, (4) cyclic and rotating disk voltammetry data for **3a** and **3c**, (5) solid-state EPR data, (6) solution EPR spectra, (7) Cartesian coordinates for optimized geometries and total energies of **I**, $\mathbf{I}^-$, **IIIa**, $\mathbf{IIIa}^-$, **IIIc**, and $\mathbf{IIIc}^-$, (8) and compiled crystallographic information file (CIF). This material is available free of charge via the Internet at http://pubs.acs.org.

IC801434H